Science Translational Medicine AAAS

Submitted Manuscript: Confidential template updated: February 28 2012

Sensitization to immune checkpoint blockade through activation of a STAT1/NK axis in the tumor microenvironment

Authors: Rachael M. Zemek[1,2], Emma De Jong[3,†], Wee Loong Chin[2,4,5,†], Iona S. Schuster[6,7,8], Vanessa S. Fear[2,4], Thomas H. Casey[1,2], Cath Forbes[2,4], Sarah J. Dart[1,2], Connull Leslie[9], Ayham Zaitouny[10,11], Michael Small[10,11], Louis Boon[12], Alistair R.R. Forrest[13], Daithi O Muiri[13], Mariapia A. Degli-Esposti[6,7,8], Michael J. Millward[4,5], Anna K. Nowak[2,4,5], Timo Lassmann[3], Anthony Bosco[3], Richard A. Lake[1,2], W. Joost Lesterhuis[1,2*]

Affiliations:

[1]School of Biomedical Sciences, University of Western Australia, M503, Crawley, WA 6009, Australia

[2]National Centre for Asbestos Related Diseases, 5th Floor QQ Block, 6 Verdun Street, Nedlands, WA 6009, Australia

[3]Telethon Kids Institute, University of Western Australia, PO Box 855, West Perth WA 6872, Australia

[4]Medical School, University of Western Australia, M503, Crawley, WA 6009, Australia

[5]Department of Medical Oncology, Sir Charles Gairdner Hospital, Hospital Ave, Nedlands, WA 6009, Australia

[6]Immunology and Virology Program, Centre for Ophthalmology and Visual Science, University of Western Australia, 35 Stirling Highway, Crawley, WA 6009, Australia

[7]Centre for Experimental Immunology, Lions Eye Institute, 2 Verdun Street, Nedlands, WA 6009, Australia

[8]Infection and Immunity Program and Department of Microbiology, Biomedicine Discovery Institute, Monash University, VIC 3800, Australia

[9]Department of Anatomical Pathology, PathWest Laboratory Medicine, QEII Medical Centre, Western Australia, Australia

[10]School of Mathematics and Statistics, University of Western Australia, 35 Stirling Highway, Crawley, WA 6009, Australia

[11]CSIRO, Mineral Resources, 26 Dick Perry Ave, Kensington, WA, 6152, Australia

[12]Bioceros, Yalelaan 46, Alexander Numan Building, 3584 CM Utrecht, The Netherlands

[13]Harry Perkins Institute of Medical Research, QQ Block, QEII Medical Centre, 6 Verdun Street, Nedlands, WA 6009, Australia

*Email: willem.lesterhuis@uwa.edu.au

†These authors contributed equally

One Sentence Summary: A STAT1-driven inflammatory phenotype associated with response to checkpoint blocking antibodies can be therapeutically attained and sensitizes cancers to immunotherapy.

Abstract:

Cancer immunotherapy using antibodies that target immune checkpoints has delivered outstanding results. However, responses only occur in a subset of patients and it is not fully understood what biological processes determine an effective outcome. This lack of understanding hinders the development of rational combination treatments. We set out to define the pretreatment microenvironment associated with an effective outcome by utilizing the fact that inbred mouse strains bearing monoclonal cancer cell line-derived tumors respond in a dichotomous manner to immune checkpoint blockade (ICB). We compared the cellular composition and gene expression profiles of responsive and non-responsive tumors from mice before ICB, and validated the findings in cancer patient cohorts treated with antibodies targeting the PD-1/PD-L1 pathway. We found that responsive tumors were characterized by an inflammatory gene expression signature consistent with upregulation of STAT1 and TLR3 signaling, and down-regulation of IL-10 signaling. In addition, responsive tumors had more infiltrating activated natural killer (NK) cells, which were necessary for response. Pretreatment of different mouse strains with large established tumors, using a combination of the STAT1-activating cytokine IFNγ, the TLR3 ligand poly(I:C) and an anti-IL-10 antibody sensitized tumors to ICB by attracting IFNγ-producing NK cells into the tumor, resulting in increased cure rates. Our results identify a pretreatment cellular and molecular tumor microenvironment that predicts response to ICB, which can be therapeutically attained. This data anticipates a biomarker-driven approach to patient management to establish whether a patient would benefit from treatment with sensitizing therapeutics before ICB.

Introduction:

Immunotherapy has become a remarkable success story in the treatment of cancer (*1*). In particular, treatment with monoclonal antibodies targeting immune checkpoint molecules such as PD-1 and CTLA-4 improves survival in patients with melanoma, non-small cell lung cancer and several other cancer types (*2-4*). However, a large proportion of patients do not benefit, and some cancer types seem to be less sensitive to immune checkpoint blockade (ICB) than others (*5, 6*). Some patients have an immediate and complete regression of all their tumors, sometimes within weeks (*7*), while other patients do not experience any therapeutic response whatsoever (*6*).

Although several correlates of response to ICB have been reported, such as expression of checkpoint ligands (*8*), mutational load (*9*), neoantigen expression (*10*), interferon signatures (*11*) and an inflammatory tumor microenvironment (*12*), no definitive predictive biomarkers have been identified (*6*). More importantly, it is unclear if it is possible to manipulate a non-responsive tumor microenvironment towards a responsive phenotype. Consequently, the clinical development of combination therapies is largely empiric, and sometimes based on scant preclinical data (*13, 14*). With over 1000 currently active clinical trials involving ICB worldwide (*15*), there is a need to prioritize immunotherapy combinations, preferably based on preclinical data, as to limit patient exposure to futile treatments and potentially severe side-effects (*5*).

Ideally, this would involve therapeutically altering the tumor microenvironment to a favorable phenotype before therapy, allowing subsequent assessment of the tumor state to define a go/no go signal for subsequent checkpoint-targeted treatment. This would not only improve prioritization of immunotherapeutic combinations to test in patients but also allow patient stratification in experimental trials and clinical practice.

Here, we made use of the fact that even in the highly homogeneous setting of inbred mouse strains bearing tumors derived from monoclonal cancer cell lines, there remains a dichotomy in responsiveness to treatment with immune checkpoint blockade (*6, 16-21*). Against this highly uniform background, we asked whether we could identify a signature in tumors before treatment that would correlate with response, and whether we could use that information to turn non-responders into responders. Using flow cytometry and bulk and single cell RNAseq data from tumors derived from two different mouse cancer models, we mapped the key cellular and molecular networks associated with response, the results of which were corroborated in several datasets of cancer patients treated with immune checkpoint blockade (*22, 23*). We prioritized upstream regulators for therapeutic targeting with drugs, recombinant proteins or antibodies, and found that we could indeed drive the tumor microenvironment from a non-responsive into a responsive state.

Results

Tumors derived from clonal cancer cell lines, grown in inbred mouse strains display two distinct gene signatures, predicting sensitivity to ICB

There are many potential reasons why a definitive biomarker for the response to ICB has not emerged, including differences in host genetics, environmental factors and the diverse genetic and cellular make up of cancers between patients (*22, 24*). Even inbred mouse strains bearing transplantable tumors display a dichotomous outcome after immunotherapy (fig. 1A)(*16-21*). This is surprising since the genomes of these mice are nominally identical. In addition, the tumors are derived from a clonal cell line, excluding the possibility that a difference in tumor rejection antigen expression caused these disparate responses. Mice are age- and gender-matched, kept under controlled conditions, and receive identical treatment. Yet, they respond very differently. Differences in outcomes between animals are possibly related to differences in T cell repertoire, which is not completely encoded in the germline (*25*), or to stochastic immunological events (*26*). Regardless of the cause of this dichotomy, we reasoned that this model would allow us to assess potentially small differences in microenvironmental regulation of therapeutic responses in a controlled background. We inoculated mice bilaterally with either AB1 mesothelioma cells or Renca kidney cancer cells and treated them with anti-CTLA-4 and anti-PD-1L ICB antibodies, which resulted in symmetric, yet dichotomous responses (fig. 1B and C). These models thus allow the biological assessment of a whole tumor at any time point, by surgically removing it, while still being able to infer the therapeutic fate of that tumor if it had been left *in situ*, by monitoring the fate of the remaining contralateral tumor (*16*). We used this model to characterize the pretreatment tumor microenvironment. We surgically removed one tumor for analysis using either bulk RNAseq, flow cytometry or single cell RNAseq shortly before administering ICB. The remaining tumor was assessed for therapeutic outcome (fig. 1D).

Using principle component analysis (PCA) of the bulk RNAseq data, we found that responsive and non-responsive tumors clustered separately in both models, (fig. 1E and F). Unsupervised

hierarchical clustering of the top differentially expressed genes also resulted in a clear separation of responsive and non-responsive tumors (fig. 1G and H, data file S1). Thus, untreated, ostensibly identical tumors in inbred mice displayed a surprising heterogeneity in gene expression profiles, differentiating animals that were going to be responders from non-responders even before they were treated with immunotherapy.

ICB responsive tumors are characterized by an inflammatory microenvironment, driven by STAT1

We aimed to gain insight into the biological relevance of the differentially expressed genes in responsive and non-responsive tumors. Firstly, we noted a striking difference between the two models in terms of differentially expressed genes between responders and non-responders, with AB1 having more than 10,000 genes differentially expressed, while in Renca only 127 genes were differentially expressed. However, the majority of the 127 genes in Renca overlapped with AB1 (118 genes), resulting in a refined response-associated signature (data file S1).

To further characterize the overarching biological processes associated with this signature, we analyzed the distribution of a well-characterized and curated collection of 'hallmark' gene sets using gene set enrichment analysis (GSEA)(*27*) (fig. 2A and fig. S1). This revealed enrichment of genes associated with a type I and II interferon response and an inflammatory environment in responsive tumors in both murine models. These gene sets were also enriched in pretreatment tumors from a cohort of urothelial cancer patients treated with PD-L1 antibody atezolizumab that went on to respond (*23*) (fig. 2B), validating the translational relevance of the findings. Pathway analysis of the common differentially expressed genes in the two models identified antigen presentation and Th1 type immune responses as the most enriched pathways in responsive tumors (fig. 2C). These data accord with published data in human melanoma (*11*), and suggest that the activation of inflammatory pathways, in particular the IFN response, renders tumors sensitive to ICB in animal cancer models and patients alike.

Next, we used weighted gene correlation network analysis (WGCNA) (*28*) to map the molecular networks underlying responsiveness to ICB. This identified 7 modules of highly co-expressed genes operating within tumors, of which one was significantly upregulated in responsive tumors in both models (module 1 in fig. 2D and fig. S2, dashed line p 0.05). This response-associated module was enriched for genes involved in immunity, including NK cell mediated cytotoxicity, PD-1 signaling and costimulation (fig. S3). Using Network Analyst (*29*) we assembled a putative network that identified *Stat1* as a hub (fig. 2E). These findings were corroborated in single cell analysis of AB1 tumors, which identified greater *Stat1* gene expression in both immune and non-immune cells (fig. S4). In addition, there was a significant (p 0.019) enrichment of a STAT1 signature in responsive tumors from the urothelial cancer/atezolizumab cohort (*23*) as well as in a second cohort of patients with melanoma treated with nivolumab (p 0.044) (*22*) (fig. 2F, fig. S5**)**. Since STAT1 is activated through phosphorylation, which can be assessed by immunohistochemistry, we assessed total and phosphorylated STAT1 abundance in our mouse models and found that responsive tumors had significantly higher percentages of positive cells than non-responsive tumors (p 0.001) (fig. 2G, H, fig. S6). Similarly, the absence of a STAT1 gene signature in human pretreatment samples was associated with a decreased progression-free survival in the urothelial cancer/atezolizumab clinical dataset (fig. S5C), which accords with a previous report on the predictive value of tumor STAT1 activation in melanoma patients treated

with anti-PD1 (*30*). Together, these data suggest that STAT1 activation is a driver of the ICB response-associated tumor microenvironment and can serve as a potential biomarker to identify patients more likely to respond.

Cellular analyses of resistant and sensitive tumors identify the presence of NK cells as a prerequisite for response to ICB

As we observed an enrichment of genes associated with an inflammatory IFN/STAT1-driven environment in responsive tumors, and because it has been previously found that 'hot' tumors are characterized by increased CD8 T cell infiltration (*30*), we examined the immune cell infiltrates of responsive and non-responsive tumors. We employed flow cytometry on dissociated tumors and compared the data with a CIBERSORT analysis (*32*); CIBERSORT is a deconvolution approach for characterizing cell composition of complex tissues that we applied to our RNAseq data. AB1 tumors were characterized by a predominantly myeloid infiltrate, whilst the infiltrate in Renca tumors was mostly lymphoid (fig. 3A, B). Interestingly, despite the striking differences in cellular infiltrates, these models respond similarly to checkpoint blockade. We did not observe any consistent difference between responders and non-responders with regard to infiltrating CD8 or CD4 T cells, B cells, macrophages, monocytic cells or dendritic cells (fig. 3A and B, fig. S7, data file S2). However, there was a greater proportion of NK cells (flow cytometry) and activated NK cells (CIBERSORT) in responding tumors in both models (fig. 3C and D). The percentage of overall leukocytes (identified as $CD45^+$ cells by flow cytometry) was the same in responsive and non-responsive tumors (fig. S8A). The percentage of tumor-infiltrating NK cells ($CD335^+/CD3^-$) of all tumor-containing cells was significantly increased ($p < 0.0001$) in responders (fig. S8B). To assess whether tumor NK cell enrichment could be relevant in humans, we interrogated gene expression data from the urothelial cancer patient cohort, obtained prior to treatment with anti-PD-L1 (23). Using CIBERSORT we found gene sets specific for activated NK cells significantly correlated with objective radiological response (CR and PR versus PD, p 0.034) (fig. 3E, fig. S9), similar to the mouse models. To test whether NK cell infiltration of the pretreatment tumor microenvironment was required for response in our models, we depleted NK cells with a single injection of anti-asialo GM1 three days before ICB in both AB1 and Renca models, which resulted in a significantly (p 0.0185 and < 0.0001 respectively) diminished response (fig. 3F, G). These data show that very different cellular tumor microenvironments between models are still conducive to a response to ICB. Furthermore, pretreatment tumor NK cell infiltration is a common prerequisite for response to ICB.

Rational development of a pretreatment combination therapy to sensitize tumors to ICB

Having identified genes differentially expressed in responsive tumors, we then rationalized that by targeting the regulators of these genes, we could induce non-responsive tumors to respond to ICB. We employed upstream regulator analysis (URA) (*33*) to identify higher-level regulators of the inflammatory pathways and networks enriched in responsive tumors. URA identifies transcriptional regulators that, based on prior experimental data, might be expected to account for the genes that are differentially expressed. Despite the marked difference in the number of differentially expressed genes and cellular infiltrates between the models, the regulators associated with response were highly similar, with the most significant ($p< 0.0001$) positive

regulators being IFNγ and STAT1, and IL-10RA the top negative regulator (fig. 4A, dashed line p 0.05, fig. S10). Importantly, the patient cohort showed similar results (fig. 4B, fig. S11). Having identified a regulator signature associated with response, we reasoned that by targeting these regulators predicted to phenocopy this signature before ICB, we could convert non-responsive to responsive tumors. We focused on therapeutics that are clinically readily available (at least in phase II clinical trials), and therefore chose a pretreatment schedule of IFNγ, anti-IL-10, and/or TLR3 agonist poly(I:C), which was also one of the top regulators and is known to activate STAT1 (*34*). We administered a short course of these treatments, for three days only, followed by ICB two days later (fig. 4C). In addition to the models previously described, we also used AE17 mesothelioma and B16 melanoma-bearing C57BL/6 mice, as both are relatively resistant to ICB (*35*). In all cases, we observed that mice pretreated with the triple combination were sensitized to ICB, with significantly increased response rates, from 0-10% with ICB alone, to up to 80% for the combination therapy (Renca $p< 0.0001$, AB1 p 0.0362, AE17 p 0.002, B16 p 0.0002) (fig. 4D to G),

To determine whether this was the effect of a single drug or due to the predicted complex treatment combination, mice were pretreated with each selected therapeutic alone followed by ICB, to which we observed no added benefit to ICB alone (fig. 4H). Although pretreatment with a combination of Poly(I:C) and either IFNγ or anti-IL-10 resulted in sensitization of some tumors, the triple combination was superior (fig. 4I). Next, to determine whether the triple combination was indeed sensitizing the tumor to ICB, rather than enforcing the effector response, we changed the scheduling and compared the triple combination followed by ICB (fig. 4C) to ICB followed by the triple combo (fig. 4J). When checkpoint blockade was given first, followed by the triple combination, response rates were similar to ICB alone. When the combination was given first, even though start of ICB was substantially delayed compared to the controls, the tumors had been sensitized and responded to therapy, in both Renca (fig. 4K) and AB1 (fig. S12). These data show that a rational complex combination of multiple clinically available therapeutics results in marked sensitization to ICB.

Sensitizing treatment induces the responsive phenotype and is dependent on NK cells

To test whether the sensitizing therapeutic combination induced the response-associated phenotype, we analyzed the tumors by flow cytometry for STAT1 activation and NK infiltration after 3 days of pretreatment with IFNγ, poly(I:C) and anti- IL10, or vehicle controls (fig. 5A). Indeed, we found that the sensitizing pretreatment significantly (AB1 p 0.079, Renca p 0.0002) increased the frequencies of $CD335^{+}$ cells (fig. 5B, S13A). In addition, there was an increase in phospho-STAT1 positive and IFNγ-producing leukocytes infiltrating the tumors (fig. 5C to D,). In addition, the pretreatment increased PD-L1, pSTAT1 and MHC-I expression on tumor cells (fig 5E, S13B and C). Although the pre-treatment-induced increase in IFNγ production was derived from multiple leukocyte subsets in the tumor, this was significant for the NK cell population only ($p < 0.0001$), not for the other cell subsets (fig. 5F). This was also the case for phosphorylation of STAT1 (fig. 5G, p 0.027). To confirm that the triple combination, rather than a single agent was driving this response phenotype, we assessed the effect of each agent alone compared to the triple combination. We found that the triple combination was superior over single treatments in terms of increased NK cell infiltration, IFNγ production and STAT1phosporylation (fig S14). Furthermore, recruitment of NK cells was greatest 1-3 days after the final dose of the triple combination, suggesting it would be optimal to start ICB early

after pre-treatment (fig S15). Further phenotypic characterization of these CD335$^+$ NK cells in the tumor revealed that they were conventional NK cells, and not tissue-resident CD335$^+$ ILC1 or ILC3 (fig. S16)(*36*). High expression of markers CD11b and KLRG1 confirmed activation and maturity of these conventional NK cells (fig 5H, I). When we depleted NK cells prior to pretreatment, we completely abolished the sensitizing effect to ICB (fig. 5J), suggesting that indeed this was mediated through treatment-induced infiltration of circulating NK cells in the tumor microenvironment. To further substantiate the role of STAT1 in the sensitizing effect of the triple combination therapy, we functionally inactivated the STAT1 pathway using blocking antibodies against IFNγ/IFNAR, which are both upstream of STAT1. This significantly diminished tumor NK cell infiltration after triple combination therapy (p 0.002) (fig S17). Together, these data show that the triple combination therapy attracts conventional NK cells into the tumor microenvironment in a STAT1-dependent manner, resulting in sensitization to subsequent ICB

Discussion

Together, our data demonstrate that a pretreatment tumor microenvironment dominated by infiltrating activated NK cells and an inflammatory gene expression signature characterized by STAT1 activation is sensitive to ICB and that this profile can be therapeutically induced. These data point to a two-step approach to treating cancer patients, in which tumor profiling allows a decision to treat initially with ICB or after pretreatment with sensitizing therapeutics (fig.5H).

We have previously argued that the therapeutic response to ICB can be visualized as a critical transition, moving from a pretreatment cancer state towards a normal tissue state (*6*). Since complex systems that display critical transitions tend to be highly sensitive to initial conditions (*37*), we set up our mouse models so that in a highly homogenous background and under controlled conditions we would still observe dichotomous outcomes, with a proportion of mice displaying a full cure and a proportion no response whatsoever. We presumed that we would find little if any difference in pre-treatment gene expression between responsive and non-responsive tumors (*6*). To our surprise however, although indeed in the Renca model only a little over hundred genes were differentially expressed between responders and non-responders, this was markedly different for AB1, where despite the homogenous background and clonality of the tumors several thousands of genes were differentially expressed. Our data thus uncover a striking immunological heterogeneity prior to treatment in subcutaneous tumor models derived from clonal cell lines in inbred mouse strains, which are widely used in cancer biology and drug discovery. It is likely that this will influence results for immunotherapy studies or other treatments such as chemotherapy, which are influenced by immunological mechanisms (*38*).

Additionally, we noted large differences in the cellular make-up of the Renca and AB1 tumors, despite them displaying a similar response rate to ICB. Our data indicate that ICB-sensitive, inflammatory ('hot') tumors are not only characterized by markedly increased numbers of immune cells such as CD8$^+$ T cells (*30*), but that discrete differences in cell populations, such as NK cells, or activation state (as measured by STAT1 activation) can be associated with major consequences in gene expression and thus sensitivity to ICB, which can be therapeutically attained.

Limitations of our analysis include the fact that we have focused on transcriptional events and thus will have missed other mechanisms that drive the response. In addition, we have only taken

a single snapshot of the pre-treatment state, so future studies will need to address the temporal immunological effects associated with the therapeutic response, for example using bilateral tumor models (*6*). We acknowledge that some effects appear to be more pronounced in the mouse models compared to the human datasets, such as the correlation between NK numbers and response. This is likely related to the heterogeneity of patients, their cancers and environmental factors, while in our mouse models those factors are all controlled, allowing the detection of small differences that would otherwise have gone unnoticed. We can also not exclude that differences in cancer type as well as the antibodies tested may have resulted in slight differences in the importance of the identified regulators between the mouse models and human datasets.

With many different immune checkpoint inhibitors currently available, in addition to other antibodies, cytokines, and small molecule drugs targeting the immune system or cancer cells, there is an abundance of choice for combination therapies. Currently these combinations are tested in many thousands of patients in the context of clinical trials, not infrequently with little preclinical rationale (*5, 15, 39*). Particularly when more than two drugs are given together, the number of potential combinations becomes prohibitive for testing in clinical trials. In this context, we showed that effective complex combinations of therapeutics can be identified by systems analysis of gene expression data from responding and non-responding tumors, and we identified a treatment combination that sensitizes tumors to ICB very effectively in multiple difficult to treat preclinical models. Our data will provide a resource for further investigating the biology associated with response to ICB and for identification of combination treatments in the context of immuno-oncology.

Study design

Our primary objective was to define the pretreatment microenvironment associated with an effective outcome by comparing gene expression and flow cytometry data from ICB responsive and non-responsive tumors within the same mouse cancer model. Our secondary objective was to test whether we could therapeutically alter the tumor microenvironment towards a responsive phenotype, and thus increase the response to ICB. By implanting a tumor s.c. on both flanks of the mouse, we were able to remove one entire tumor 1 hour prior to therapy with ICB, then monitor the remaining tumor for response. The removed tumor was analyzed by flow cytometry, bulk RNAseq or single cell RNAseq, and categorized as a responsive or non-responsive tumor based on the outcome of the corresponding tumor left *in situ*. Tumors that had an intermediate response (partial response or relapse) were excluded from analysis. We performed these experiments using AB1 mesothelioma and Renca renal cell carcinoma cell lines. In order to exclude model-specific effects, we focused on genes that were differentially expressed between responsive and non-responsive tumors in both models. The sample size for the bulk RNAseq experiments was estimated using the method developed by Hart et al (*40*).

We then used this transcriptomic data to identify pathways and regulators that could be targeted. We validated the findings using publicly available RNAseq data from two cancer patient cohorts (*22, 23*). We utilized *in vivo* targeting studies with tumor growth as an endpoint. These studies were performed in BALB/c mice carrying AB1 and Renca tumors, and were validated in unrelated s.c AE17 mesothelioma and B16 melanoma models in C57BL/6 mice, to establish robustness across tumor models and mouse strains. Mice were randomized after tumors were established, prior to tumor removal and therapy. Treatments were administered by one

researcher, while tumors were measured by another researcher who was blinded for treatment allocation.

Supplementary Materials

References and Notes:

1. W. J. Lesterhuis, J. B. Haanen, C. J. Punt, Cancer immunotherapy - revisited. *Nat Rev Drug Discov* **10**, 591-600 (2011).
2. F. S. Hodi *et al.*, Improved Survival with Ipilimumab in Patients with Metastatic Melanoma. *New Engl J Med* **363**, 711-723 (2010).
3. M. Reck *et al.*, Pembrolizumab versus Chemotherapy for PD-L1-Positive Non-Small-Cell Lung Cancer. *N Engl J Med* **375**, 1823-1833 (2016).
4. J. D. Wolchok *et al.*, Nivolumab plus ipilimumab in advanced melanoma. *N Engl J Med* **369**, 122-133 (2013).
5. O. The Lancet, Calling time on the immunotherapy gold rush. *Lancet Oncol* **18**, 981 (2017).
6. W. J. Lesterhuis *et al.*, Dynamic versus static biomarkers in cancer immune checkpoint blockade: unravelling complexity. *Nat Rev Drug Discov* **16**, 264-272 (2017).
7. P. B. Chapman, S. P. D'Angelo, J. D. Wolchok, Rapid eradication of a bulky melanoma mass with one dose of immunotherapy. *N Engl J Med* **372**, 2073-2074 (2015).
8. R. S. Herbst *et al.*, Predictive correlates of response to the anti-PD-L1 antibody MPDL3280A in cancer patients. *Nature* **515**, 563-567 (2014).
9. M. Yarchoan, A. Hopkins, E. M. Jaffee, Tumor Mutational Burden and Response Rate to PD-1 Inhibition. *N Engl J Med* **377**, 2500-2501 (2017).
10. E. M. Van Allen *et al.*, Genomic correlates of response to CTLA-4 blockade in metastatic melanoma. *Science* **350**, 207-211 (2015).
11. M. Ayers *et al.*, IFN-gamma-related mRNA profile predicts clinical response to PD-1 blockade. *J Clin Invest* **127**, 2930-2940 (2017).
12. R. R. Ji *et al.*, An immune-active tumor microenvironment favors clinical response to ipilimumab. *Cancer Immunol Immunother* **61**, 1019-1031 (2012).
13. S. Farkona, E. P. Diamandis, I. M. Blasutig, Cancer immunotherapy: the beginning of the end of cancer? *BMC Med* **14**, 73 (2016).
14. Rationalizing combination therapies. *Nat Med* **23**, 1113 (2017).
15. J. Tang, A. Shalabi, V. M. Hubbard-Lucey, Comprehensive analysis of the clinical immuno-oncology landscape. *Ann Oncol* **29**, 84-91 (2018).
16. W. J. Lesterhuis *et al.*, Network analysis of immunotherapy-induced regressing tumours identifies novel synergistic drug combinations. *Sci Rep* **5**, 12298 (2015).
17. S. Chen *et al.*, Combination of 4-1BB agonist and PD-1 antagonist promotes antitumor effector/memory CD8 T cells in a poorly immunogenic tumor model. *Cancer Immunol Res* **3**, 149-160 (2015).
18. S. R. Woo *et al.*, Immune inhibitory molecules LAG-3 and PD-1 synergistically regulate T-cell function to promote tumoral immune escape. *Cancer Res* **72**, 917-927 (2012).
19. R. P. Sutmuller *et al.*, Synergism of cytotoxic T lymphocyte-associated antigen 4 blockade and depletion of CD25(+) regulatory T cells in antitumor therapy reveals alternative pathways for suppression of autoreactive cytotoxic T lymphocyte responses. *J Exp Med* **194**, 823-832 (2001).
20. M. A. Curran, W. Montalvo, H. Yagita, J. P. Allison, PD-1 and CTLA-4 combination blockade expands infiltrating T cells and reduces regulatory T and myeloid cells within B16 melanoma tumors. *Proceedings of the National Academy of Sciences of the United States of America* **107**, 4275-4280 (2010).

21. J. F. Grosso, M. N. Jure-Kunkel, CTLA-4 blockade in tumor models: an overview of preclinical and translational research. *Cancer immunity* **13**, 5 (2013).
22. N. Riaz *et al.*, Tumor and Microenvironment Evolution during Immunotherapy with Nivolumab. *Cell* **171**, 934-949 e915 (2017).
23. S. Mariathasan *et al.*, TGFbeta attenuates tumour response to PD-L1 blockade by contributing to exclusion of T cells. *Nature* **554**, 544-548 (2018).
24. W. Hugo *et al.*, Genomic and Transcriptomic Features of Response to Anti-PD-1 Therapy in Metastatic Melanoma. *Cell* **168**, 542 (2017).
25. A. Madi *et al.*, T cell receptor repertoires of mice and humans are clustered in similarity networks around conserved public CDR3 sequences. *Elife* **6**, (2017).
26. R. N. Germain, The art of the probable: system control in the adaptive immune system. *Science* **293**, 240-245 (2001).
27. A. Liberzon *et al.*, The Molecular Signatures Database (MSigDB) hallmark gene set collection. *Cell Syst* **1**, 417-425 (2015).
28. P. Langfelder, S. Horvath, WGCNA: an R package for weighted correlation network analysis. *BMC Bioinformatics* **9**, 559 (2008).
29. J. Xia, M. J. Benner, R. E. Hancock, NetworkAnalyst--integrative approaches for protein-protein interaction network analysis and visual exploration. *Nucleic Acids Res* **42**, W167-174 (2014).
30. P. C. Tumeh *et al.*, PD-1 blockade induces responses by inhibiting adaptive immune resistance. *Nature* **515**, 568-571 (2014).
31. M. A. Care, D. R. Westhead, R. M. Tooze, Gene expression meta-analysis reveals immune response convergence on the IFNgamma-STAT1-IRF1 axis and adaptive immune resistance mechanisms in lymphoma. *Genome Med* **7**, 96 (2015).
32. A. M. Newman *et al.*, Robust enumeration of cell subsets from tissue expression profiles. *Nat Methods* **12**, 453-457 (2015).
33. A. Kramer, J. Green, J. Pollard, Jr., S. Tugendreich, Causal analysis approaches in Ingenuity Pathway Analysis. *Bioinformatics* **30**, 523-530 (2014).
34. J. Dempoya *et al.*, Double-stranded RNA induces biphasic STAT1 phosphorylation by both type I interferon (IFN)-dependent and type I IFN-independent pathways. *J Virol* **86**, 12760-12769 (2012).
35. S. I. Mosely *et al.*, Rational Selection of Syngeneic Preclinical Tumor Models for Immunotherapeutic Drug Discovery. *Cancer Immunol Res* **5**, 29-41 (2017).
36. E. Vivier *et al.*, Innate Lymphoid Cells: 10 Years On. *Cell* **174**, 1054-1066 (2018).
37. M. Scheffer *et al.*, Anticipating critical transitions. *Science* **338**, 344-348 (2012).
38. A. M. Cook, W. J. Lesterhuis, A. K. Nowak, R. A. Lake, Chemotherapy and immunotherapy: mapping the road ahead. *Curr Opin Immunol* **39**, 23-29 (2016).
39. J. Kaiser, Too much of a good thing? *Science* **359**, 1346-1347 (2018).
40. S. N. Hart, T. M. Therneau, Y. Zhang, G. A. Poland, J. P. Kocher, Calculating sample size estimates for RNA sequencing data. *J Comput Biol* **20**, 970-978 (2013).
41. W. J. Lesterhuis *et al.*, Synergistic effect of CTLA-4 blockade and cancer chemotherapy in the induction of anti-tumor immunity. *PLoS One* **8**, e61895 (2013).
42. D. Aran *et al.*, Reference-based annotation of single-cell transcriptomes identifies a profibrotic macrophage niche after tissue injury. *BioRxiv*, 284604 (2018).
43. S. Andrews, FastQC: A Quality Control tool for High Throughput Sequence Data. *Available online at: https://www.bioinformatics.babraham.ac.uk/projects/fastqc/*, (2010).

44. D. Kim, B. Langmead, S. L. Salzberg, HISAT: a fast spliced aligner with low memory requirements. *Nat Methods* **12**, 357-360 (2015).
45. M. Lawrence *et al.*, Software for Computing and Annotating Genomic Ranges. *PLOS Computational Biology* **9**, e1003118 (2013).
46. M. Pertea *et al.*, StringTie enables improved reconstruction of a transcriptome from RNA-seq reads. *Nature biotechnology* **33**, 290-295 (2015).
47. A. C. Frazee *et al.*, Ballgown bridges the gap between transcriptome assembly and expression analysis. *Nature biotechnology* **33**, 243-246 (2015).
48. S. Anders, W. Huber, Differential expression analysis for sequence count data. *Genome Biology* **11**, R106 (2010).
49. M. I. Love, W. Huber, S. Anders, Moderated estimation of fold change and dispersion for RNA-seq data with DESeq2. *Genome Biology* **15**, 550 (2014).
50. Y. Benjamini, Y. Hochberg, Controlling the False Discovery Rate: A Practical and Powerful Approach to Multiple Testing. *Journal of the Royal Statistical Society. Series B (Methodological)* **57**, 289-300 (1995).
51. D. Szklarczyk *et al.*, STRING v10: protein-protein interaction networks, integrated over the tree of life. *Nucleic Acids Res* **43**, D447-452 (2015).
52. Z. Chen *et al.*, Inference of immune cell composition on the expression profiles of mouse tissue. *Scientific reports* **7**, 40508 (2017).
53. A. C. Frazee *et al.*, Flexible isoform-level differential expression analysis with Ballgown. *bioRxiv*, (2014).
54. A. Subramanian, H. Kuehn, J. Gould, P. Tamayo, J. P. Mesirov, GSEA-P: a desktop application for Gene Set Enrichment Analysis. *Bioinformatics* **23**, 3251-3253 (2007).
55. F. Reynier *et al.*, Importance of correlation between gene expression levels: application to the type I interferon signature in rheumatoid arthritis. *PLoS One* **6**, e24828 (2011).

Figure captions:

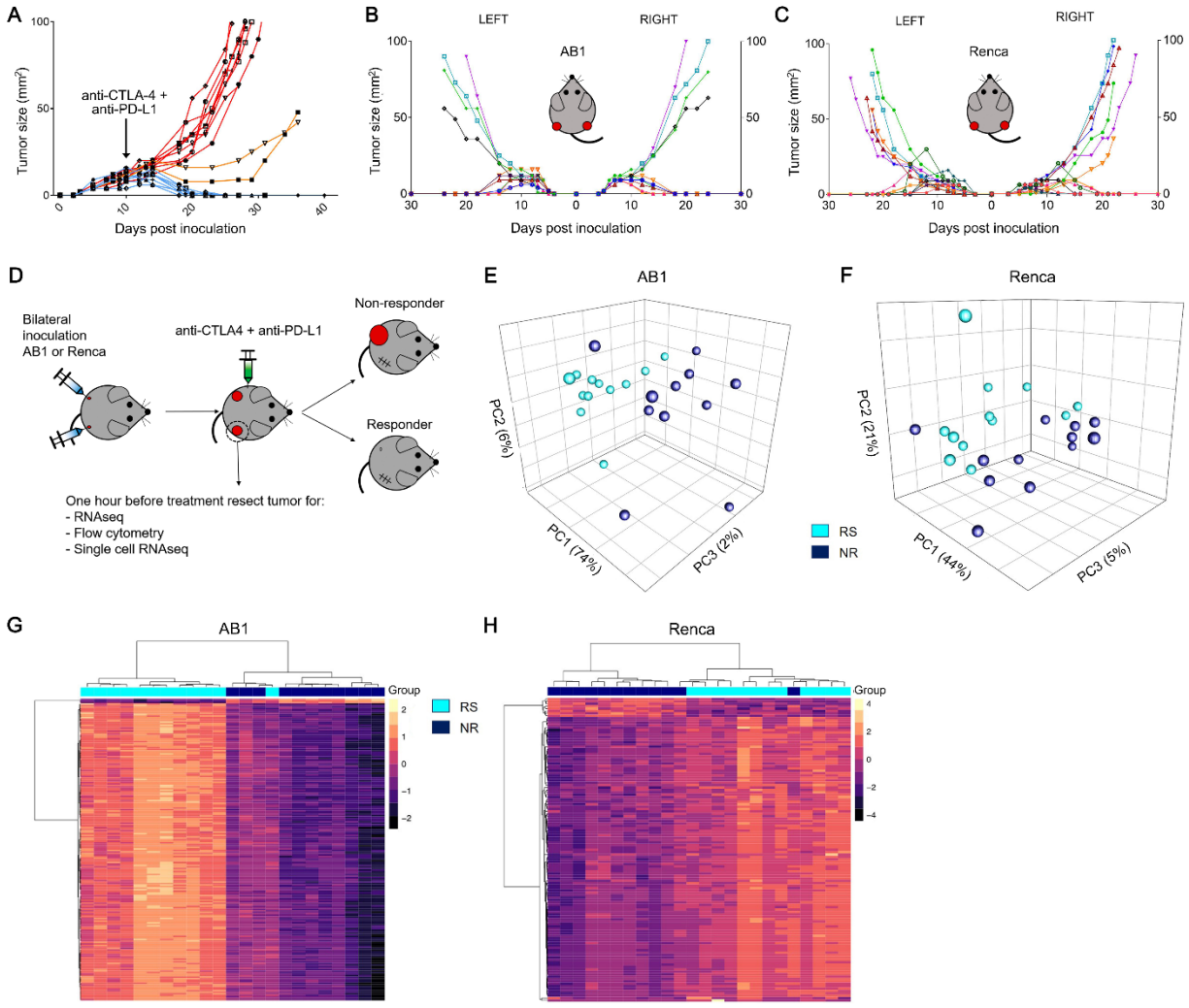

Fig. 1. Inbred mouse strains, carrying monoclonal tumors display a symmetrical, yet disparate response to ICB, associated with a distinctive gene signature. (**A**) Representative Renca tumor growth curves showing ICB non-responders (red), intermediate responders (orange) and responders (blue) to ICB. (**B** and **C**) Representative growth curves of mice with bilateral AB1 tumors (**B**) or Renca tumours (**C**) treated with ICB, (n =10) color-coded per mouse. (**D**) Experimental design. (**E** and **F**) PCA of responsive (RS) and non-responsive (NR) AB1 tumors (**E**) and Renca tumors (**F**) (n = 12/group). (**G** and **H**) Unsupervised hierarchical clustering of top differentially expressed genes separating responsive and non-responsive tumors. For AB1 (**G**), 10307 genes were differentially expressed in responders versus non-responders (top 200 shown), and 127 genes for Renca (**H**) (all shown, also see **data file S1**).

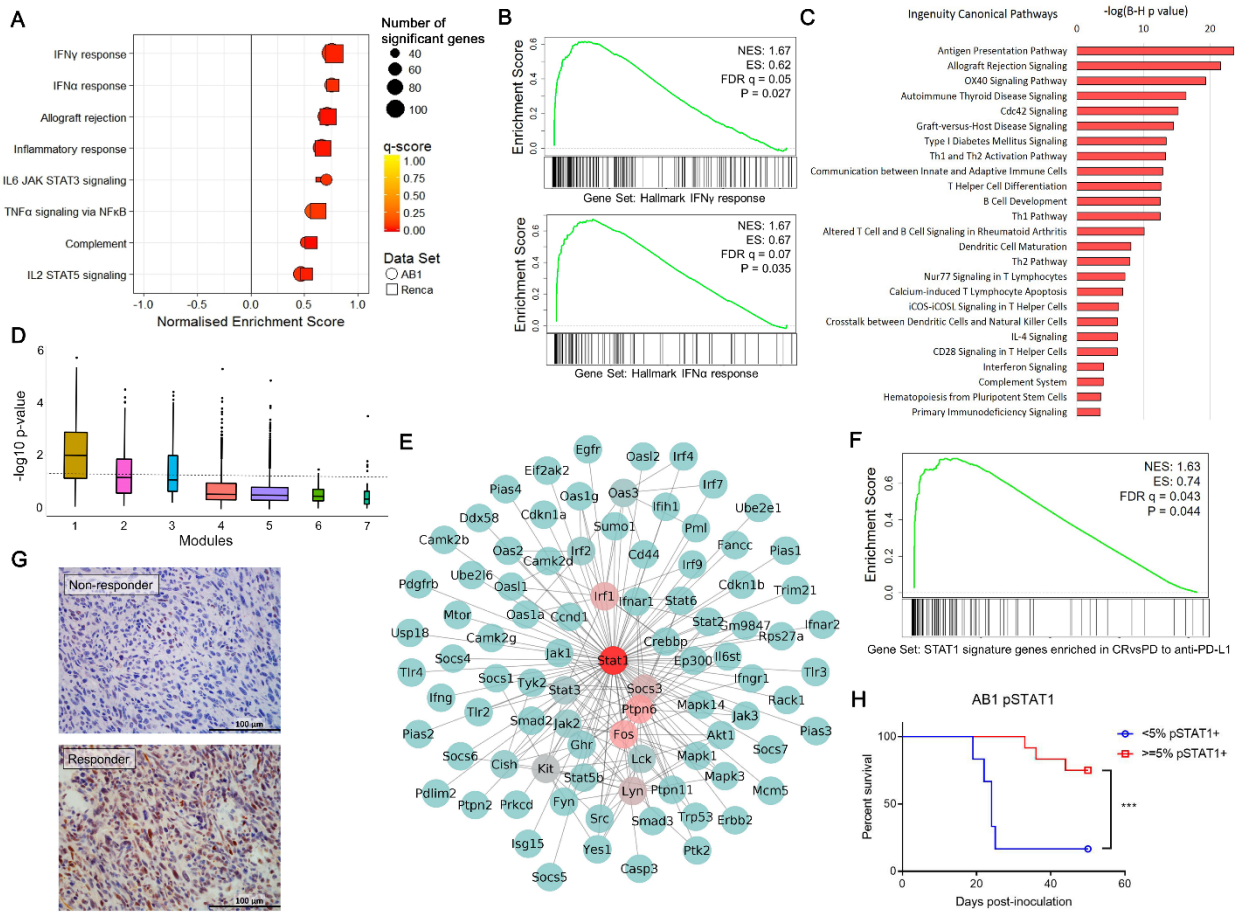

Fig. 2. Inflammatory pathways with STAT1 as a key regulator are enriched in ICB responsive tumors in mouse models and patients. (**A**) GSEA top hallmark gene sets in responsive versus non-responsive tumors. (**B**) GSEA of responsive versus non-responsive tumors from the patient cohort (n = 192)(*23*). (**C**) Over-represented canonical pathways within responsive tumors. (**D**) WGCNA module enrichment for differentially expressed genes between responsive and non-responsive tumors. Bars = SD with outliers, Horizontal line p = 0.05. (**E**) Prior knowledge-based graphical reconstruction of the wiring diagram of module 1 (**F**) GSEA of responsive (complete response) versus non-responsive (progressive disease) tumors from the patient cohort (n = 192)(*23*), using a STAT1 gene set (*31*). (**G**) Representative pSTAT1 immunohistochemistry in non-responsive and responsive AB1 tumors. Scale bar = 100 μm (**H**) Survival curves of pSTAT1 high and low ICB treated tumors (n = 10 RS, 8 NR; Logrank test, ***p < 0.001).

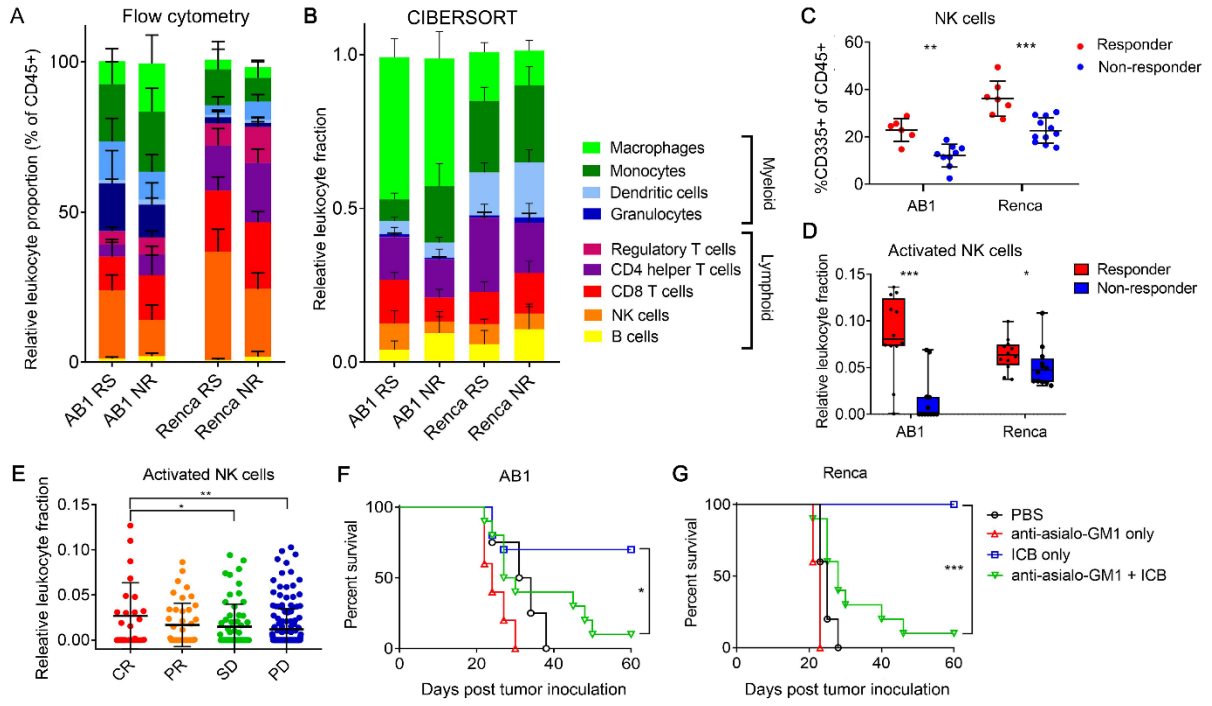

Fig. 3. NK cells are enriched in ICB sensitive tumors in mouse models and patients and are required for response. (**A**) Flow cytometry of dissociated tumors from responsive (n = 6) and non-responsive (n = 9) AB1, or responsive (n = 7) and non-responsive (n = 11) Renca tumor-bearing mice. (**B**) CIBERSORT analysis from responsive and non-responsive tumors (n = 12/group). (**C**) NK cells ($CD335^{+}$) in responsive and non-responsive tumors shown in **A**. (**D**) NK fraction relative to total leukocyte infiltrate by CIBERSORT (Mann-Whitney U test with Benjamini-Hochberg correction for multiple comparisons). (**E**) Activated NK cell fraction (CIBERSORT) in tumors from the patient cohort. CR, complete response, PR, partial response, SD, stable disease; PD, progressive disease. (n = 298, Mann-Whitney U test, bars = standard deviation). (**F** and **G**) Survival plots of AB1 (**F**) or Renca-bearing mice (**G**) treated with ICB, with or without anti-asialo-GM1 3 days prior to start of ICB. Mice were treated early with ICB (day 5 for AB1, day 7 for Renca), allowing interrogation of response attenuation (n= 10 mice/group, 2 independent experiments, Logrank test). *p < 0.05, **p < 0.01, ***p < 0.001.

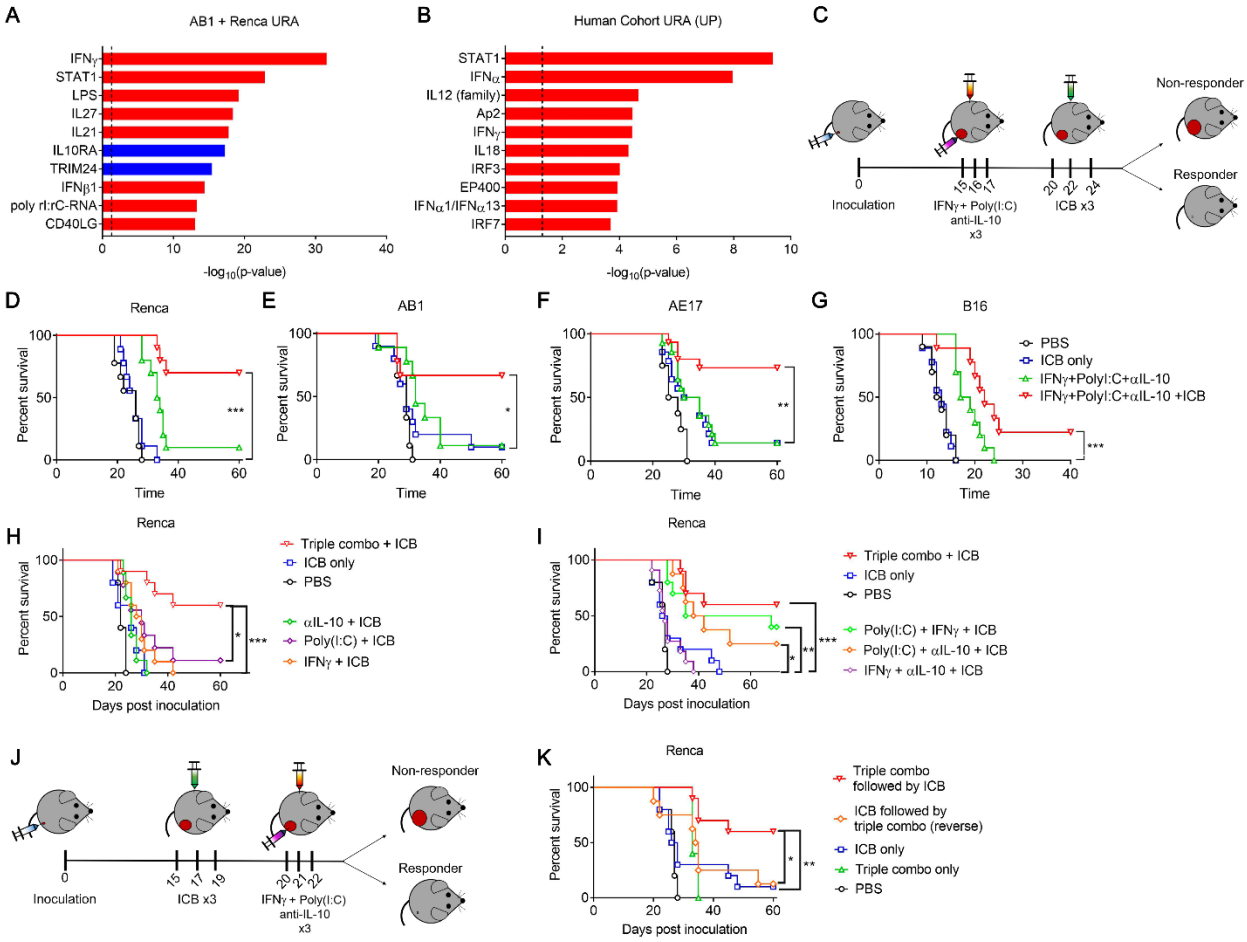

Fig. 4. Rational therapeutic modulation of the tumor microenvironment sensitizes tumors to ICB. (**A**)URA predicted regulators of the response-associated gene signature (red = positive correlation, blue = negative). (**B**) URA predicted regulators in responders versus non-responders of the patient cohort (n = 192)(*23*). (**C**) Sensitizing treatment schedule. (**D-G**) Survival curves of Renca- (**D**), AB1- (**E**), AE17- (**F**) and B16-bearing (**G**) mice treated with the triple combination (Poly(I:C) + IFNγ + anti- IL-10) followed by ICB compared to ICB alone (n = 10/group; 15 for AE17). (**H**) Survival curves of Renca-bearing mice treated with single agent therapy (anti-IL-10 or Poly(I:C) or IFNγ) versus the triple combination prior to ICB. (**I**) Survival curves of Renca-bearing mice treated with double agent therapy versus the triple combination prior to ICB (n = 10/group, 2 independent experiments of 5 mice/group; Logrank test compared to ICB only group, *p< 0.05, **p< 0.01, ***p< 0.001). (**J**) Treatment schedule to test ICB followed by triple combination therapy. (**K**) Survival curves of Renca-bearing mice treated with the triple combination followed by ICB as shown in **C,** or with the reverse schedule, as shown in **J** (n = 10/group, 2 independent experiments of 5 mice/group) (Logrank test, *p< 0.05, **p< 0.01).

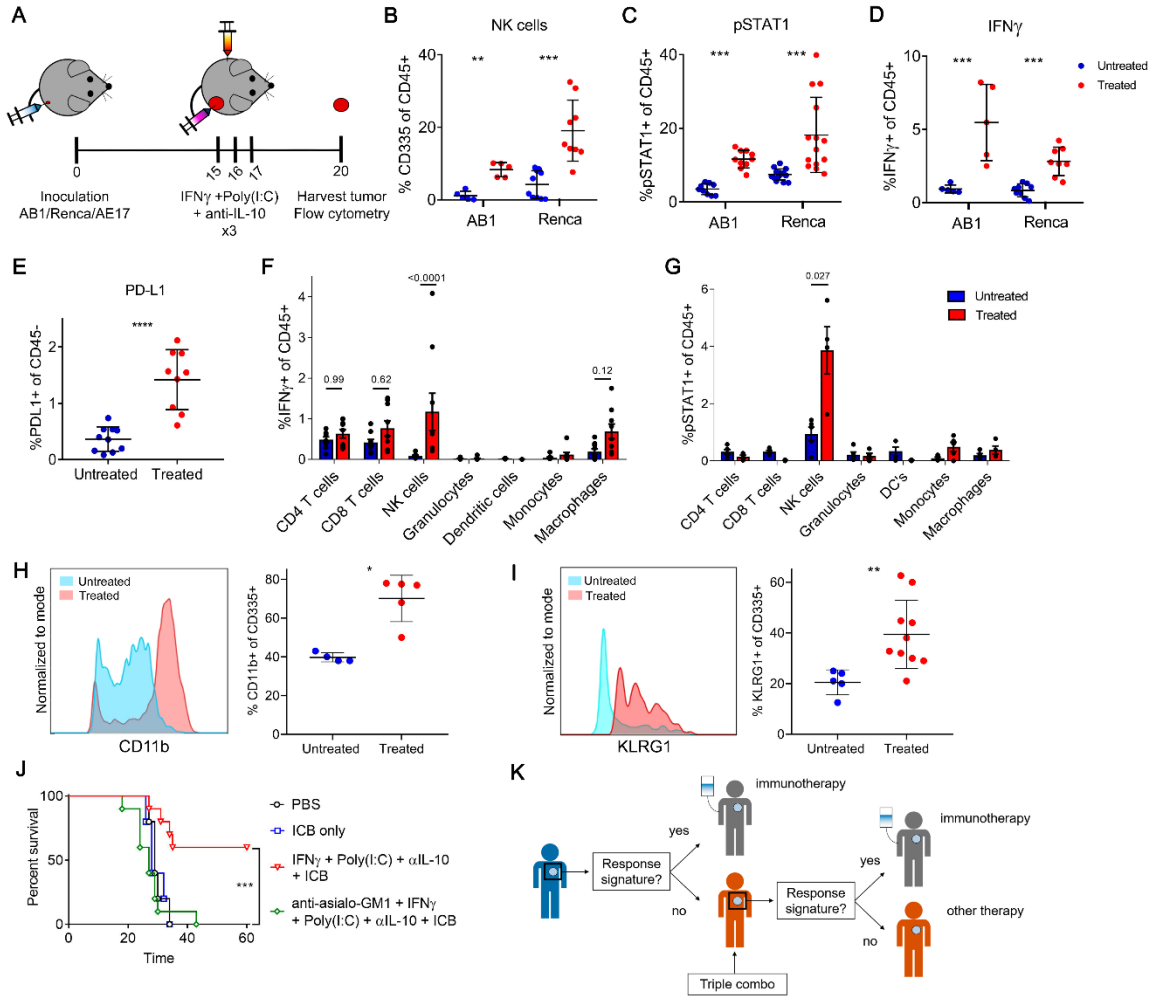

Fig. 5. Sensitizing triple therapy activates the STAT1/NK axis in the tumour microenvironment. (A) Treatment schedule and harvest for analysis by flow cytometry. (**B** to **D**) NK cell fraction (**B**), STAT1 activation (**C**), and IFNγ production (**D**) by $CD45^+$ tumor-infiltrating leukocytes, and PD-1L expression by $CD45^-$ non-leukocytes (**E**) after treatment with IFNγ, Poly(I:C) and anti-IL-10 (Mann-Whitney U test, bars= standard deviation, *p < 0.05, **p < 0.01, ***p < 0.001). (**F,G**) , IFNγ expression (**F**) and STAT1 phosphorylation (**G**) in tumor-infiltrating lymphocytes ($CD45^+$ cells) (Mann-Whitney U test) *p< 0.05, **p< 0.01 (**H,I**) CD11b (**H**) and KLRG1 (**I**) expression by $CD335^+$ NK cells in tumors from Renca-bearing mice after 3-day treatment with PBS (untreated) or IFNγ, Poly(I:C) and anti-IL-10 (treated). (**J**) Survival curves of Renca-bearing mice, receiving sensitization followed by ICB, with or without NK-depleting anti-asialo-GM1 antibody (n = 10/group; n = 5 PBS controls; Logrank test, ***p < 0.001). (**K**) Proposal for an adaptive treatment approach.

Acknowledgments: The authors acknowledge the facilities, and the scientific and technical assistance of the Australian Microscopy & Microanalysis Research Facility at the Centre for Microscopy, Characterisation & Analysis, The University of Western Australia, a facility funded by the University, State and Commonwealth Governments. Cell line Renca was kindly donated by Dr E. Sotomayor and Dr F. Cheng (University of South Florida, Tampa, FL). We thank Cuong To, Caitlin Tilsed, Catherine Rinaldi, Pauline Deng and Danika Hope for technical assistance and Ian Dick for statistical advice.

Funding: This work was funded by project grant 1103980 from the National Health and Medical Research Council (NHMRC). W.J.L is funded by an NHMRC RD Wright Fellowship and a Fellowship from the Cancer Council of Western Australia. W.L.C. is funded by a Western Australian Cancer and Palliative Care Network fellowship. M.A.D-E is funded by an NHMRC Principal Research Fellowship. A.Z. is funded by Discovery Project DP180100718 by the Australian Research Council. Part of this research was made possible using equipment funded by the Australian Cancer Research Foundation to establish the ACRF Centre for Advanced Cancer Genomics and with the support of a collaborative cancer research grant provided by the Cancer Research Trust.

Author contributions: R.M.Z. performed and interpreted all mouse experiments, flow cytometry experiments, GSEA and ingenuity pathway analyses, and co-wrote the paper. E.D.J. performed and interpreted the bulk RNAseq analyses, upstream regulator analysis and WGCNA. W.L.C. performed and interpreted the computational analyses of the human RNAseq data. I.S.S. and M.A.D-E developed, designed and performed the IFNy and NK/ILC flow cytometry panels, interpreted the data and aided in manuscript preparation. V.F., C.F. and T.C. provided technical assistance with surgery and in vivo treatment experiments. S.H. and C.L. designed, performed and analyzed the pSTAT1 immunohistochemistry. L.B. provided critical reagents and aided in manuscript preparation. A.R.R.F. and D.O.M. designed and performed the single cell RNAseq experiments. R.A.L., M.J.M. and A.K.N. were involved in experimental design and interpretation of all in vivo studies, the flow cytometry experiments and the human dataset analysis, and critical revision of the manuscript. T.L. and W.L.C. performed and interpreted all analyses pertaining to single cell RNAseq data. T.L. supervised and interpreted the computational analysis of the human RNAseq dataset and critically revised the manuscript. A.B. was involved in experimental design of the murine RNAseq experiments, supervised, and together with T.L., A.Z and M.S. interpreted the computational analyses of bulk RNAseq data and critically revised the manuscript. W.J.L. designed the study, developed the models, interpreted all data and supervised the project. R.M.Z and W.J.L. wrote the manuscript with input from all authors. All authors gave final approval of the version to be published.

Competing interests: Patent application pertaining to aspects of this work: R.M.Z, W.J.L., R.A.L. and A.B. (2018900962, 'Method for immunotherapy drug treatment'). A.K.N., M.J.M., A.B., R.A.L., W.J.L.: research funding and consultancy for Douglas Pharmaceuticals. W.J.L. research funding from Astra Zeneca. A.K.N. advisory boards for Boehringer Ingelheim, Bayer Pharmaceuticals, Roche Pharmaceutics, Bristol Meyers Squib; research funding from Astra Zeneca. MM: advisory boards for Merck Sharp & Dohme, Bristol-Myers Squibb, Roche, Astra-Zeneca.

Data and materials availability: The raw RNAseq data are available from the Gene Expression Omnibus data repository (accession: GSE117358).

SUPPLEMENTARY

Materials and Methods

Mice

BALB/cArc, BALB/cJAusb and C57BL6/J mice 8-12 weeks of age were used for all experiments. Mice were obtained from the Animal Resource Centre (Murdoch, WA), or the Australian BioResources (Moss Vale, NSW) and housed at the Harry Perkins Institute of Medical Research Bioresources Facility under specific pathogen free conditions. Mice were fed Rat and Mouse cubes (Specialty Feeds) and had access to water *ad libitum*. Cages (Techniplast) were individually ventilated with filtered air, contained aspen chips bedding (Tapvei) and were supplemented with tissues, cardboard rolls and wood blocks as environmental enrichment. Cages were changed every 14 days. Mice were housed at 21-22°C with 12-hour light/dark cycle (06:00 – 18:00). Sentinel mice (n = 3) in the animal facility were screened monthly for a standard panel of bacteria and fungi, ectoparasites, endoparasites, non-pathogenic protozoa and viruses (Cerberus Sciences). All experiments were conducted in compliance with the institutional guidelines provided by the Harry Perkins Institute for Medical Research animal ethics committee (approval numbers AE047, AE091).

Cell culture

Cell lines AB1 and AE17 were obtained from CellBank Australia. Cell line Renca was kindly donated by Dr E. Sotomayor and Dr F. Cheng (University of South Florida, Tampa, FL). Cell line B16 was obtained from ATCC (CRL-6475). Cell lines were maintained in RPMI 1640 (Invitrogen) supplemented with 20 mM HEPES, 0.05 mM 2-mercaptoethanol, 100 units/ml penicillin (CSL), 50 μg/ml gentamicin (David Bull Labs), and 10% FCS (Invitrogen). Cells were grown to 70-80% before passage and passaged 3-5 times before inoculation. Cells were frequently tested for mycoplasma by PCR and remained negative. Cell lines were validated yearly by flow cytometry for MHC class I molecules H2-K^b (consistent with C57BL/6) and H2-K^d (consistent with BALB/c), and for fibroblast markers E-cadherin, Epithelial cell adhesion molecule and platelet-derived growth factor receptor α (negative) and by PCR for mesothelin (positive for AB1, negative for Renca).

In vivo treatments

When cell lines were 70-80% confluent, they were harvested and washed 3 times in PBS. 5 x 10^5 cells in 100 μl were inoculated subcutaneously (s.c.) onto the lower right-hand side (RHS) flank (for single inoculations) or both flanks (for dual tumor inoculations) using a single 26G needle per injection. Mice were randomized when tumors became palpable, approximately 3-5 days after tumor inoculation. Treatments were administered by one investigator (RMZ), while tumors were measured at least 3 times weekly using calipers by a researcher (TC) who was blinded for treatment allocation, to guarantee blinded assessment of the primary endpoint.

Surgery experiments

Seven (AB1) or 10 (Renca) days post tumor inoculation, when tumors were ~ 9 mm^2, mice were dosed with 0.1 mg/kg buprenorphine in 100 µl s.c. (30 min prior) and anesthetized using isoflurane (4% in 100% oxygen at a flow rate of 2 L/min). Whole tumors and the corresponding draining inguinal lymph node on the RHS were removed by surgical excision and immediately immersed in RNAlater (Life Technologies) for RNAseq, or cold PBS for single cell RNAseq or flow cytometry. The wound was closed with staples (Able Scientific-). Mice were placed in a heat box for recovery. One hour after surgery, mice were administered ICB. The remaining tumor was monitored as an indicator of response for the removed tumor. Mice were designated as responders when their tumor completely regressed and they remained tumor free for up to 4 weeks after treatment. Mice were designated as non-responders if their tumors grew to 100 mm^2 within 4 weeks after start of treatment, similar to saline-treated controls. Mice that had a delay in tumor growth or partial regression were designated as intermediate responders and excluded from the analysis. For internal consistency, we only used experiments in which mice displayed a dichotomous response; in any cage there had to be at least one non-responder amongst responders or vice versa.

In vivo ICB treatment

The anti-PD-L1 hybridoma (clone MIH5) and the anti-CTLA4 hybridoma (clone 9H10) were cultured in IMDM containing 1% of FCS and gentamycin. Clarified supernatants were used to purify the antibody using affinity chromatography. The antibody was sterile formulated in PBS. Mice received an intraperitoneal (i.p.) dose of 100 µg of anti- CTLA4 and 100 µg anti-PD-L1 combined in 100 µl phosphate-buffered solution (PBS). Mice received additional doses of 100 µg anti-PD-L1 two and four days later. In previous experiments(*41*) we had not found any difference in effect of control IgG versus PBS, and therefore vehicle controls received PBS alone. We varied the time of treatment initiation after tumor inoculation as to obtain a suitable background response rates to ICB; high for experiments in which responses were to be negated, and low in experiments in which the response rate was to be improved.

Tumor preparation for RNA sequencing:

RNAseq, flow cytometry and single cell RNAseq was performed on tumors from separate experiments. For RNAseq, whole tumors and lymph nodes were surgically resected, the surrounding tissue was removed and immediately submerged in RNAlater (Life Technologies). Samples were stored at 4°C for 24 hours, after which supernatant was removed and samples transferred to -80°C. Frozen tumors were dissociated in Trizol (Life Technologies) using a TissueRuptor (QIAgen). RNA was extracted using chloroform and purified on RNeasy MinElute columns (QIAgen). RNA integrity was confirmed on the Bioanalyzer (Agilent Technologies). Library preparation and sequencing (50 bp, single-end) was performed by Australian Genome Research Facility, using Illumina HiSeq standard protocols.

Single cell RNAseq

For single cell RNAseq, tumors were harvested, and submerged in cold PBS, cut into 1-2 mm pieces with a scalpel blade and dissociated using the GentleMACS system (Miltenyi Biotec). Single cell suspensions were stored at -80°C in 10% DMSO until processed for single cell

profiling. Cryo-stored cells were rapidly thawed and diluted in PBS and pelleted, Pellets were resuspended in PBS and passed through a 40 μM filter to remove cell clumps. Approximately 5,000 cells per sample were then loaded onto a 10x genomics Chromium controller to generate Chromium Single Cell 3' Libraries. Sequencing was carried out by the Australian Genome Research Foundation in Melbourne Australia.
Primary analysis was carried out using the 10x genomics cell ranger software suite. Raw sequencing data was de-multiplexed (cellranger v2.1.1 and bcl2fastq v2.20.0.422), reads aligned to the reference (GRCm38, Ensembl 84 build) and gene expression quantified using the cell ranger count command. Using default parameters some droplets containing real cells were discarded. We therefore used the expected-cells 6000 flag to include these cells. Responder and non-responder samples were combined using cellranger aggr function. We annotated all cells in our samples using the SingleR software package (*42*).

Flow cytometry
For flow cytometry tumors were harvested and immediately submerged in cold PBS, cut into 1-2 mm pieces with a scalpel blade and dissociated using the GentleMACS system. Fc block (anti-CD16/CD32, BD) was used for 10 minutes on ice. UV Zombie live/dead (Biolegend) was used to discriminate live cells. Cells were permeabilized and fixed using FoxP3 fix/Perm buffer kit (Biolegend) before addition of antibodies for 20 minutes at RT. See Table S1 for antibody details. Cells were kept in stabilizing fixative until acquisition. Data were acquired on a BD Fortessa flow cytometer and analyzed using FlowJo software (TreeStar).
Cell populations were defined as: Monocytes ($CD11b^+MHCII^{+/-}Ly6C^+F4/80^-CD11c^-$); Macrophages ($CD11b^+$ $MHCII^+F4/80^+CD11c^{+/-}Ly6C^-Ly6G^-$); Immature myeloid cells ($CD11b^+MHCII^-F4/80^+Ly6C^-Ly6G^-$); Neutrophils/granulocytes ($CD11b^+Ly6G^+MHC^-$ $Ly6C^{int}F4/80^-$); CD8 T cells ($CD3^+CD8^+$); CD4 helper T cells ($CD3^+CD4^+FoxP3^-$); Treg ($CD3^+CD4^+FoxP3^+$); NK cells ($CD335^+CD3^-$); and B Cells ($CD19^+CD3^-$)). See Supplementary Figure 18 for gating strategies.
For detection of IFNγ, cells were incubated with brefeldin A at 37°C for 4 hours. Fixable Viability Stain 620 (BD) was used to identify dead cells. Cells were surface stained with antibodies for 20 minutes at RT. Following permeabilization with Cytofix/Cytoperm (BD), cells were stained with anti-IFNγ (ThermoFisher) in permwash (PBS/0.1% saponin (Sigma-Aldrich)) for 30 minutes on ice.
For detection of phospho-STAT1, dissociated tumors were stained with surface antibodies, fixed with 1.5% formaldehyde for 10 minutes, then permeabilized with ice-cold methanol at 4°C for 10 minutes. Cells were stained with a rabbit-anti-pSTAT1 antibody (Tyr701) -PE (Cell Signaling Technology) for 30 minutes at RT.
For detection of intracellular NK/ILC1 markers, cells were permeabilized using FoxP3 buffer Kit (ThermoFisher). See table S1 for antibodies used.

ICB sensitizing drug dosing schedules
Dosing with pretreatment drugs commenced on day 15 for AB1 and Renca, day 10 for AE17 or day 8 for B16. IFNγ (Shenandoah Biotechnology) was dosed s.c. into tumor area at 50,000 units daily for 3 days. Poly(I:C) (HMW, Invivogen) was dosed s.c. into tumor area at 50 μg daily for 3 days. The anti-IL-10 hybridoma (clone JES5.2A5) was cultured in IMDM containing 1% of FCS and gentamycin. Clarified supernatants were used to purify the antibody using affinity

chromatography. The antibody was sterile formulated in PBS. Anti-IL-10 was dosed i.p. at 0.5 mg/mouse daily for 3 days. ICB was dosed 2 days after pretreatment drug schedule; day 20 for AB1 and Renca, day 15 for AE17 or day 13 for B16; for the ICB only group, dosing began at the same time as the pretreatment drug dosing commenced in the other arms.

NK cell depletion

To investigate the impact of NK cell depletion, ICB antibodies were administered early (day 5 (AB1) or 7 (Renca) to give a high background response rate. Anti-asialo-GM1 (Wako Chemicals) was dosed at 20 μg in 50 μl of saline, and injected i.v. 3 days prior to ICB administration (day 2 (AB1) or 4 (Renca)). NK cell depletion was verified by flow cytometric analysis of peripheral blood using antibodies for CD45 and CD335; we also used antibodies for CD3, CD4, CD8, ICOS and Ki67 found no depletion of CD8 or CD4 T cells, nor decrease in number of activated cells.

Bulk RNAseq data analysis

Read libraries were quality assessed using FastQC(*43*) (v0.11.3) and mapped to the mouse genome (mm11) at both the transcript and gene level using HISAT2(*44*) (v2.0.4). Gene-level quantitation (counts) of aligned reads was performed using SummerizeOverlaps(*45*), and transcript discovery and quantification using Stringtie(*46*) (v1.3.0) and Ballgown(*47*).

Principal component analysis (PCA) was performed to visualize the major contributions of variation within the data using the prcomp() function within R (v3.3.3). Gene count data was transformed for PCA employing the variance stabilizing transformation (*48*). The top 1000 most variable genes across samples (those with the greatest median absolute deviation) were selected for PCA. Differentially expressed genes were identified between immunotherapy non-responders and responders using DESeq2(*49*). P-values were adjusted for multiple comparisons using the Benjamini-Hochberg (B-H) method; those < 0.05 were considered significant (*50*). A full list of DE genes is in data file S1.

Differentially expressed genes were uploaded to InnateDB (www.innatedb.com) along with associated gene expression data. A list of pathways mapping to the uploaded genes was returned, and pathway analysis was undertaken to determine which pathways were significantly overrepresented ($p< 0.05$) in the up- and downregulated gene data sets. InnateDB simultaneously tests for overrepresentation of DE genes in more than 3,000 pathways, from which we looked at the KEGG (www.genome.ad.jp/kegg/), and Reactome (www.reactome.org/) databases. The Benjamini and Hochberg (BH) FDR correction was applied to correct for multiple testing.

The weighted gene co-expression network analysis (WGCNA) algorithm was used to construct a signed network across all samples and identify clusters (modules) of genes with highly correlated patterns of gene expression. To prepare the data for WGCNA we (i) applied a variance stabilizing transformation to normalize the data, (ii) filtered out genes expressed at a low level (only those with at least 10 counts per sample were retained), (iii) removed genes without an official MGI symbol and (iv) removed genes with low variability by applying the varianceBasedfilter() function within the DCGL package (significance threshold set to 0.01). The resulting set of 6026 genes were used as input for network construction. Network modules of co-expressed genes identified by WGCNA were tested for enrichment of differentially expressed

genes between immunotherapy non-responders and responders by plotting the $-\log_{10}$ p-values derived from the DESeq2 analysis, on a module-by-module basis. Protein-protein interactions of the differentially expressed genes were created using Innate DB network analysis tool (unfiltered), and network created using Network Analyst (*29*), with STRING interactome, confidence cut-off 900(*51*). Rendering of module interactions was performed with Cytoscape software. Network modules of interest and differentially expressed genes (filtered to include those with an absolute fold-change in expression > 2) were also analyzed within Ingenuity Systems (*33*) to identify associated upstream transcriptional regulators, using right-tailed Fisher's exact tests and default settings for other options. P-values < 0.05 were considered significant. An activation z-score was also calculated for each upstream transcriptional regulator by comparing their known effect on downstream targets with observed changes in gene expression. Those with activation z-scores ≥ 2 or ≤ -2 were considered "activated" or "inhibited", respectively.

The CIBERSORT (*32*) algorithm was used to estimate the relative proportions of 25 mouse hematopoietic immune cell types based on the transcriptomic profiles of each sample, where the 511 mouse-gene signature developed by Chen et al.(*52*) was used as a reference. We broadly classified the 25 cell types into 12 major populations by collapsing several related sub-populations as follows: B cells comprise memory, naïve and plasma cells; $CD8^+$ T cells comprise memory, naïve and activated cells; CD4 T cells comprise memory, naïve, follicular, Th1, Th2 and Th17 cells; Macrophages comprise M0, M1 and M2 phenotypes; NK cells comprise activated and resting cells; DCs comprise activated and immature cells. Prior to analysis, transcript level data was library size and gene length normalized using the ballgown package (*53*) resulting in Fragments Per Kilobase of transcript per Million mapped reads (FKPM). Individual transcripts were collapsed to gene level data based on the mean FPKM value using the aggregate() function. Finally, the data was filtered to retain genes with an FPKM value > 0.3 in at least 8 samples (being the smallest experimental group size).

The Broad Institute gene set enrichment analysis (GSEA) software (*54*) was used to run analyses on normalized gene expression data with prefiltering for low counts. The Hallmarks gene set database which uses 50 MSigDB Hallmarks gene sets (*27*) and a STAT1 signature were used. The STAT1 signature was derived from Care et al. (*31*), defined based on variance-ranked Spearman correlations of gene expression across 11 DLBCL datasets, selecting strongly correlated genes (cut-off median correlation score > 0.6). A total of 1000 permutations were performed. All other default parameters were used. Gene sets enriched at a nominal *P* value < 0.05 and FDR< 0.25 were considered significant.

Survival analysis for patients with STAT1 signature enrichment

To define the subset of patients with STAT1 pathway activation for survival analysis, we closely followed the Classification Algorithm Based on a Biological Signature (*55*). We used the previously defined STAT1 gene set from Care et al. (*31*) and leveraged RNAseq data from the Imvigor210 trial (*23*), available as an R data package (Imvigor210CoreBiologies). The dataset contains gene count data of 348 urothelial cancer patients treated with anti-PD-L1 antibody atezolizumab. Patients were classified by best response: 25 complete responders (CR), 43 partial responders (PR), 63 with stable disease (SD), and 167 progressors (PD). 50 patients did not have evaluable disease (NE). From this RNAseq data, two prototype vectors were defined based on

mean expression values of genes in this STAT1 gene set; a "responder" prototype from radiological complete responders and partial responders and a "progressor" prototype based on progressor samples. For each patient, expression profiles of the STAT1 gene set were compared to the two prototype vectors. Similarity was calculated based on Pearson correlation coefficient and a decision score formulated based on the ratio of correlations. This decision score was used to classify all patients in the Imvigor210 dataset regardless of response, with a decision score > 1 denoting higher activation of the STAT1 pathway. Survival analysis was performed using the Logrank test, dividing patients based on this decision score, with a decision score > 1 denoting higher activation of the STAT1 pathway; a Kaplan-Meyer survival curve was constructed.

Immunohistochemistry for STAT1 **and p** STAT1

For immunohistochemical staining of STAT1and p STAT1, slides of 4 μm thickness were cut from formalin-fixed, paraffin-embedded (FFPE) tissue blocks. Slides were deparaffinized in two changes of xylene followed by rehydration in changes of 100%, 96%, 70% and 40% ethanol and distilled water. For STAT1 staining, antigen retrieval using 10 mM citrate buffer (pH 6.0) was performed for 10 min at 121°C using a pressure cooker (Cuisinart). For p STAT1 staining, slides were sub-boiled in 1 M EDTA buffer (pH 8.0) for 10 minutes in a microwave. Slides were rinsed in TBST and the endogenous peroxidase was blocked using 3% hydrogen peroxidase (Sigma) in distilled water. Sections were washed again in TBST and blocked with goat serum (Vectastain) diluted in PBS as per manufacturer's instructions. Primary antibody, STAT1 or p STAT1 (Cell Signaling, dilution: 1/800 and 1/200 respectively), was incubated for 60 minutes at RT. Sections were washed and secondary antibody, goat anti-Rb IgG-HRP (Santa Cruz), was incubated for 30 minutes at RT, before washing again. Betazoid DAB chromogen (Biocare Medical) was prepared as per manufacturer's instructions. Chromogen was applied, sections were monitored for the development of a brown color and the reaction was stopped with H_2O. Sections were counterstained with haematoxylin and rehydrated before mounting coverslips with Pertex. An experienced pathologist (C.L.) scored the sections by assigning an estimated proportion of positive tumor cells (positivity defined as moderate or strong nuclear staining for p STAT1 and moderate or strong nuclear and cytoplasmic positivity for STAT1), while blinded to treatment outcome.

Statistics

The sample size calculation for *in vivo* mouse experiments was based on prior experiments in which we found that the median survival time on the control treatment (ICB alone) was 35 days (*16*). Using a proportional hazards model we determined that, if the true hazard ratio (relative risk) of control subjects relative to experimental subjects is 5, we would need to study 10 experimental subjects and 10 control subjects to be able to reject the null hypothesis that the experimental and control survival curves are equal with probability (power) 0.8. The type I error probability associated with this test of this null hypothesis is 0.05.

The sample size for the bulk RNAseq experiments was estimated using the method developed by Hart et al (*40*); for sample sizes of n=12 and a within group coefficient of variation of 0.3 there is >90% power to detect a 1.7-fold change in gene expression. Differences in population

frequencies in responders and non-responders using flow cytometry and CIBERSORT were determined using Mann-Whitney U testing on means.

Prism software (GraphPad) was used to analyze tumor growth and to determine statistical significance of differences between groups by applying a Mann-Whitney U test. P-values were adjusted for multiple comparisons using the Benjamini-Hochberg (B-H) method; those < 0.05 were considered significant. The Kaplan-Meir method was used for survival analysis, and p-values were calculated using the log-rank test (Mantel-Cox).

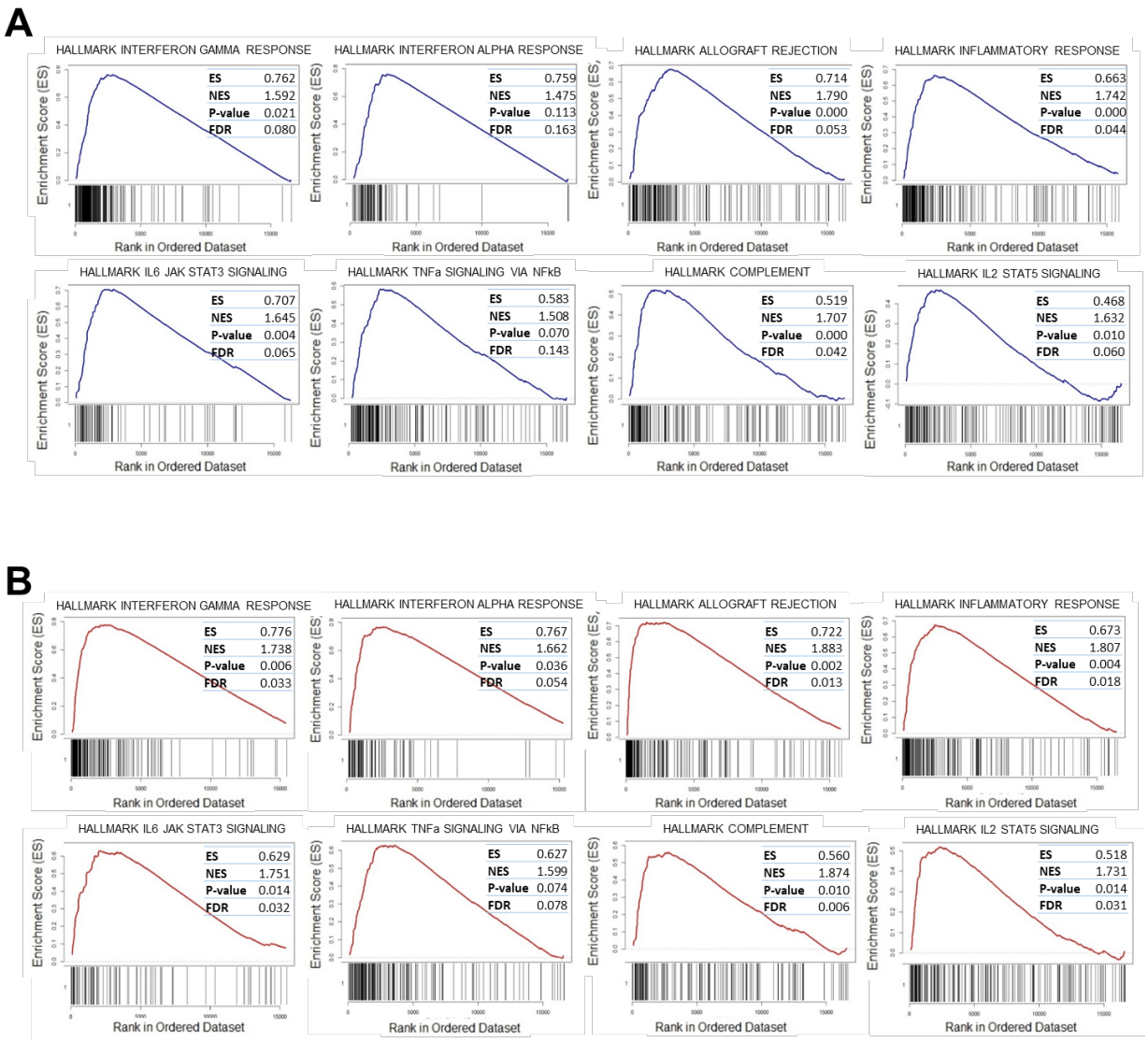

Supplementary Fig. 1: Individual Gene Set Enrichment Analysis graphs of the top 8 Hallmark gene sets in AB1 and Renca. Individual random walk graphs from both AB1 (**A**) and Renca (**B**) showing a strong association of these hallmark gene signatures in responders. In the upper right corner of each graph: NES= Normalized enrichment score, ES= Enrichment Score, FDR = False discovery rate q-score.

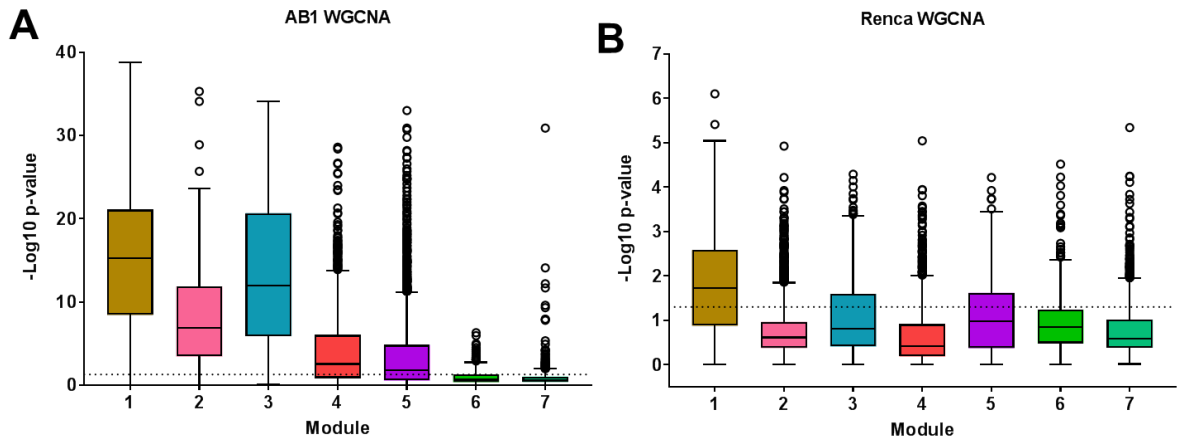

Supplementary Fig. 2: Weighted gene correlation network analysis showing expression of modules upregulated in responders in AB1 and Renca separately. Network modules overlaid onto p-values from DESeq2 analysis comparing responders to non-responders reveals which modules are associated with response. AB1 (A) demonstrated an overwhelming large differential expression in responders compared to non-responders, as reflected in 5 out of 7 modules being significantly ($p < 0.05$) associated with response. Renca (B) identified module 1 (brown) as the driver of response (box and whisker plots, whiskers 1.5 IQR) (dashed line; $p = 0.05$).

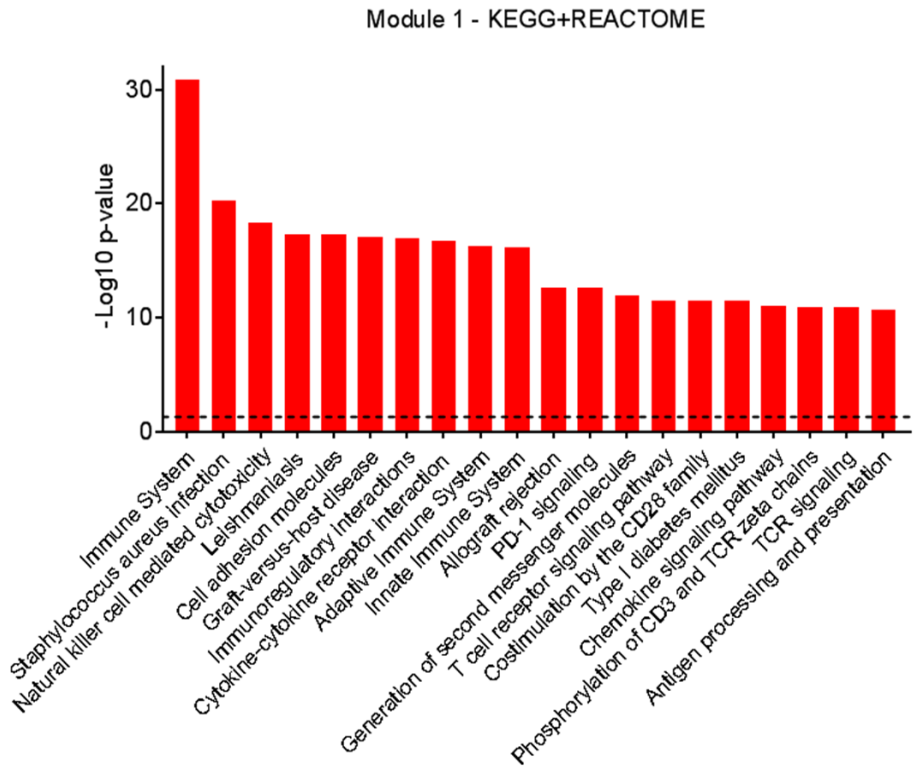

Supplementary Data Fig. 3: Reactome and KEGG pathway enrichment of response-associated module (module 1) in overlap of AB1 and Renca. Pathway analysis reveals immune-associated pathways, including NK cell-mediated cytotoxicity, reflected by the genes upregulated in the response-associated module (dashed line: p = 0.05).

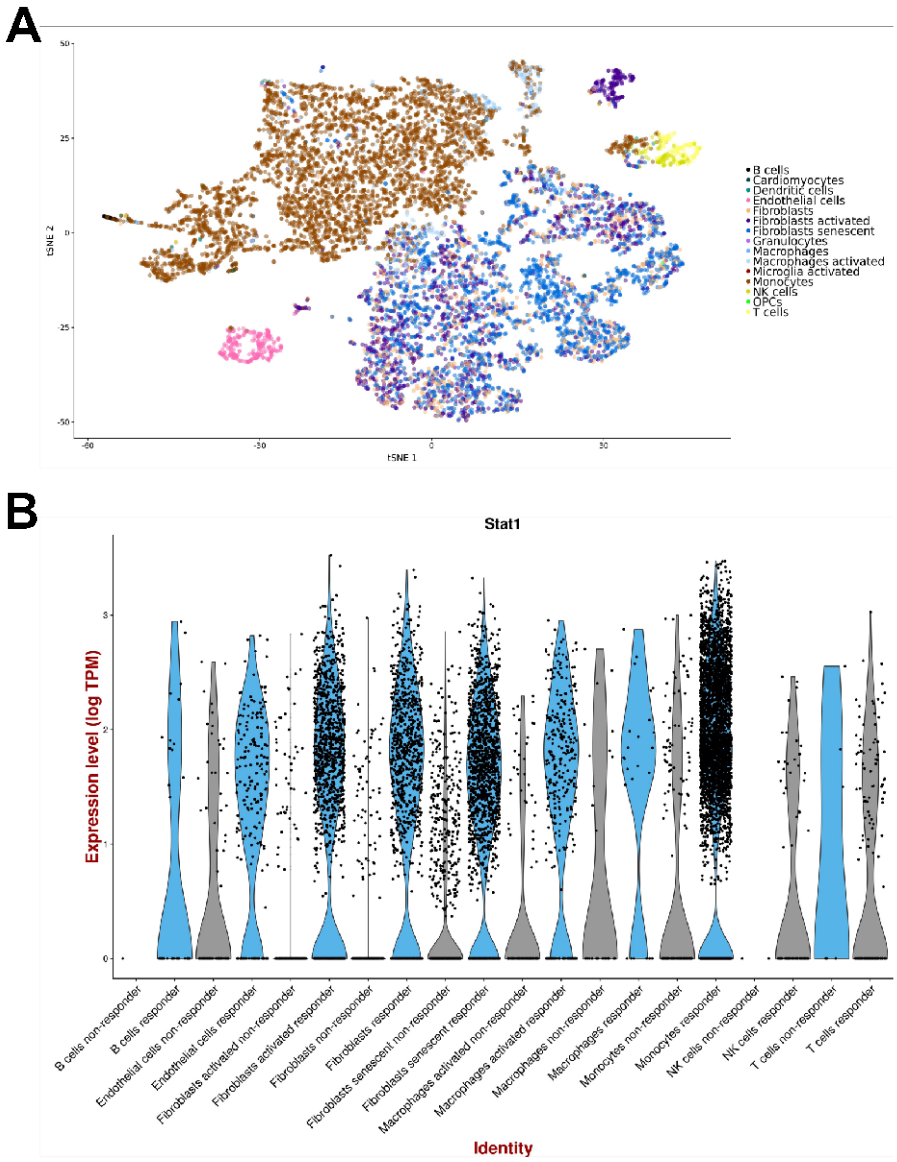

Supplementary Fig. 4: Single cell analysis of responsive/non-responsive AB1 tumors. (**A**) Transcriptomes of responsive and non-responsive AB1 tumors visualized by tSNE (10,743 cells). Cell subsets were annotated using SingleR. (**B**) Violin plot of STAT1 expression across cell types in responsive and non-responsive AB1 tumors.

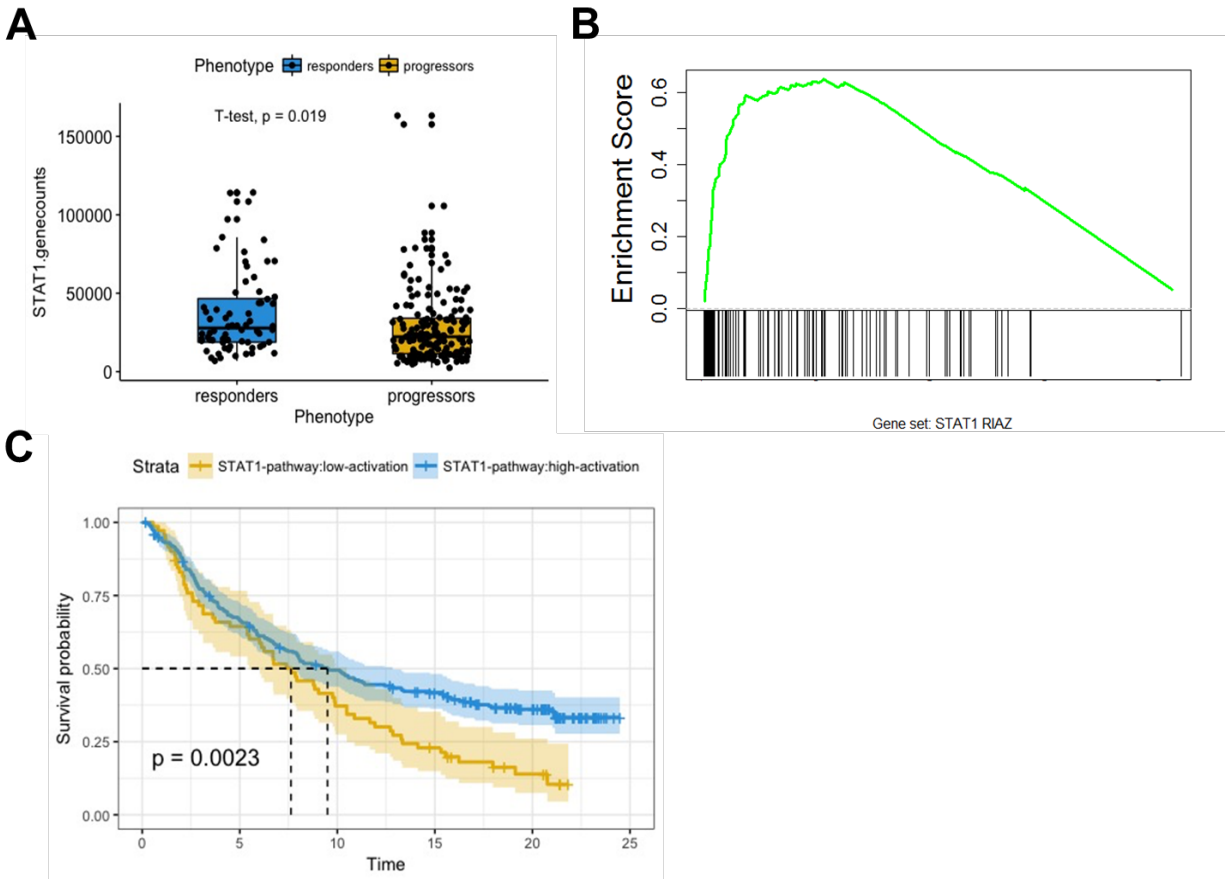

Supplementary Fig. 5: STAT1 expression and correlation with response in human patient cohorts. (**A**) STAT1 expression in responders (CR and PR) and non-responders (SD and PD) in urothelial cancer patients treated with anti-PD-L1 (*23*); n=298 with response data. (**B**) We also tested the STAT1 signature in a second cohort, of melanoma patients treated with anti-PD1 antibody nivolumab (*22*). GSEA of responsive (CR and PR =10) versus non-responsive (PD =23) tumors from a melanoma patient cohort treated with anti-PD1 (n = 33), using a STAT1 gene set. (**C**) Since we identified phosphorylated STAT1 correlated with response to ICB in mice, and we did not have the availability of prospectively collected tumor tissue from patients, we aimed to identify whether a STAT1 activation signature would be associated with response. All patients (n=348) were divided into two even groups based on their level of STAT1 activation. High STAT1 activation, as defined by a STAT1 gene set using the Classification of Biological Signatures algorithm, correlated with increased overall survival regardless of radiological response. CR, complete response; PR, partial response; SD, stable disease; PD, progressive disease.

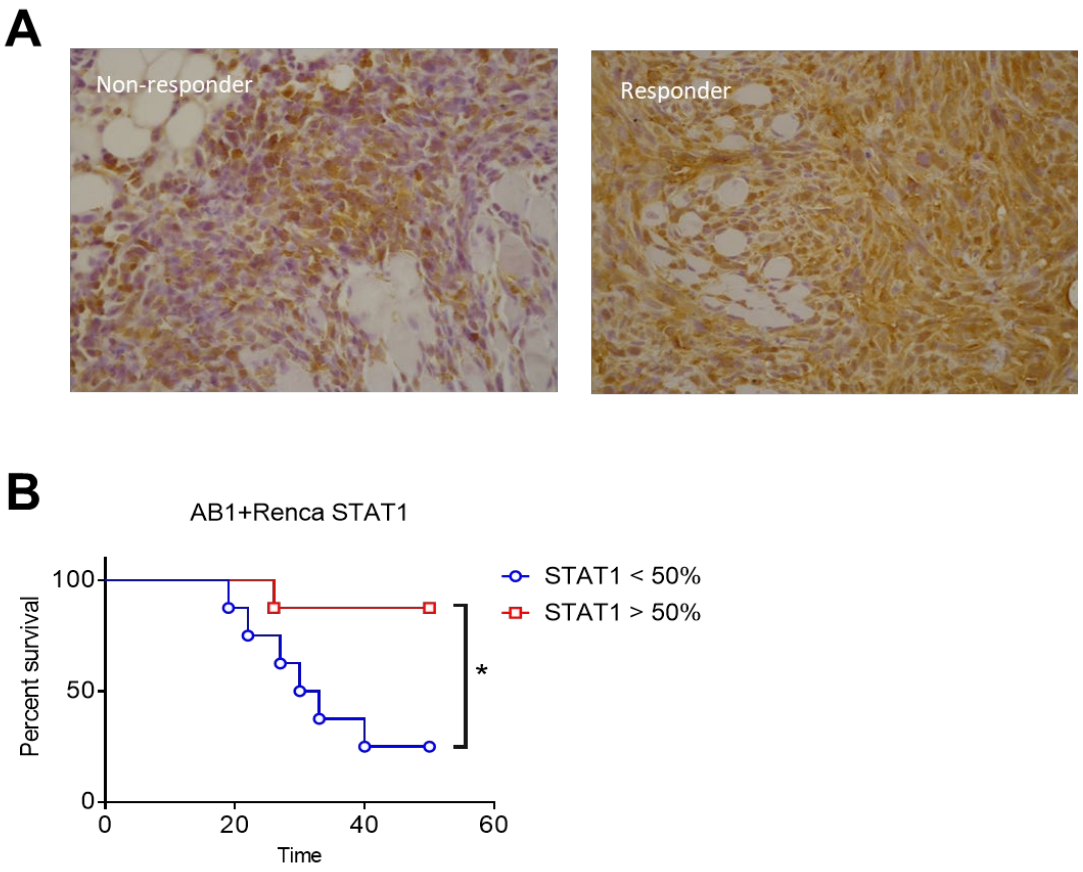

Supplementary Fig. 6: STAT1 IHC on AB1 and Renca tumors. (**A**) Representative immunohistochemical staining of total STAT1 in non-responsive (left) and responsive (right) Renca tumors. The total STAT1 staining was more difficult to assess than the pSTAT1 staining, due to STAT1 having less variability in percentage of positive cells between samples (**B**) Survival curves of STAT1 positive and negative Renca and AB1-bearing mice treated with anti-CTLA4/anti-PD-L1 (n=9 responders, 7 non-responders; Logrank test, *p< 0.05).

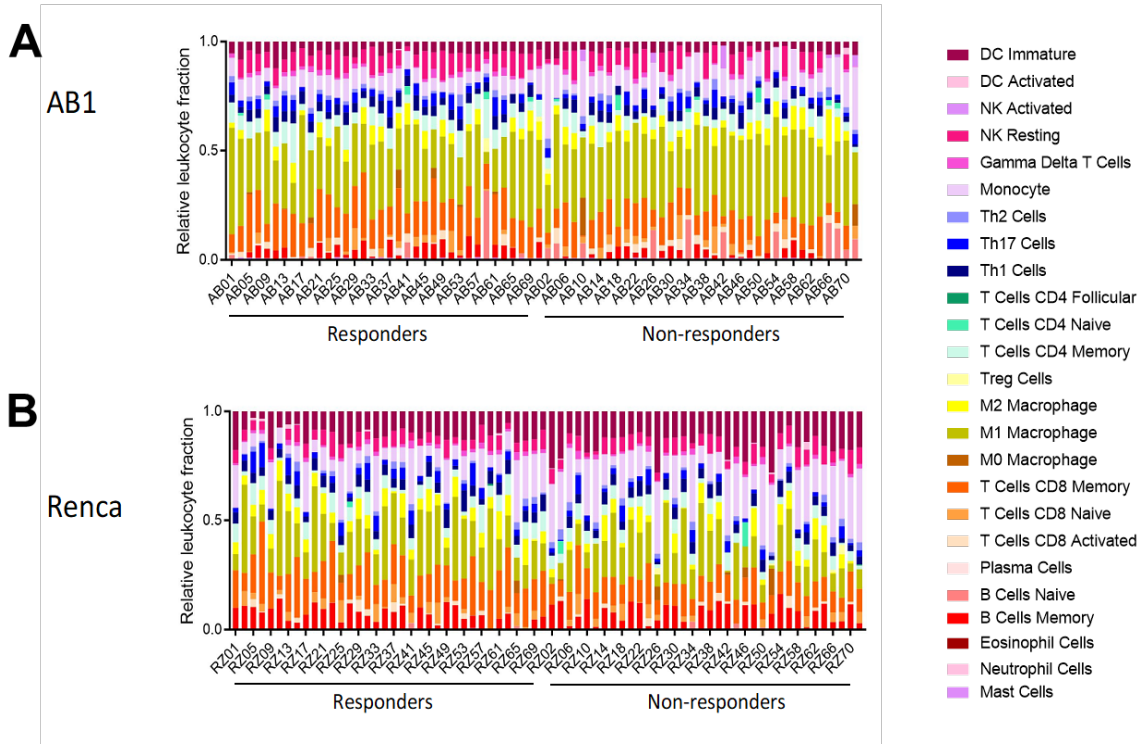

Supplementary Fig. 7: CIBERSORT of individual samples of responders and non-responders in AB1 and Renca before treatment with anti-CTLA4/anti-PD-L1. Stacked graphs of individual samples of whole AB1 (**A**) and Renca (**B**) tumors analyzed by CIBERSORT using RNA sequencing data. 25 cell subsets are discriminated as a relative proportion of the leukocytes within each sample. The two models demonstrate clear differences in cellular composition. Moreover, there is variability between individual mice, both within and between the responsive and non-responsive groups.

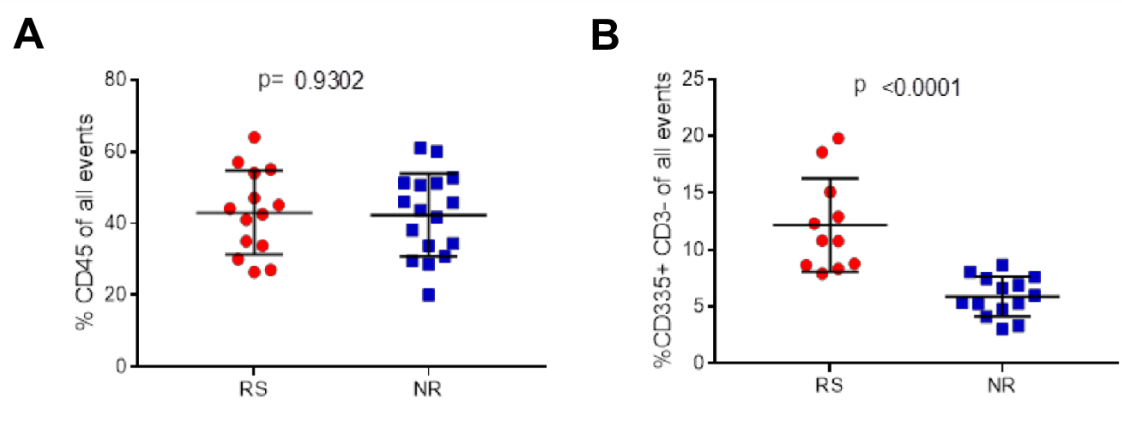

Supplementary Fig. 8: Analysis of flow cytometry cell populations as a percentage of all events. (**A**) % CD45 of total viable cells in responsive and non-responsive AB1 tumours, showing there were no differences in the number of leukocytes between responders and non-responders. (**B**) The number of NK cells as a percentage of the total events in AB1 tumours, showing NK cell number was significantly higher in responders compared to non-responders.

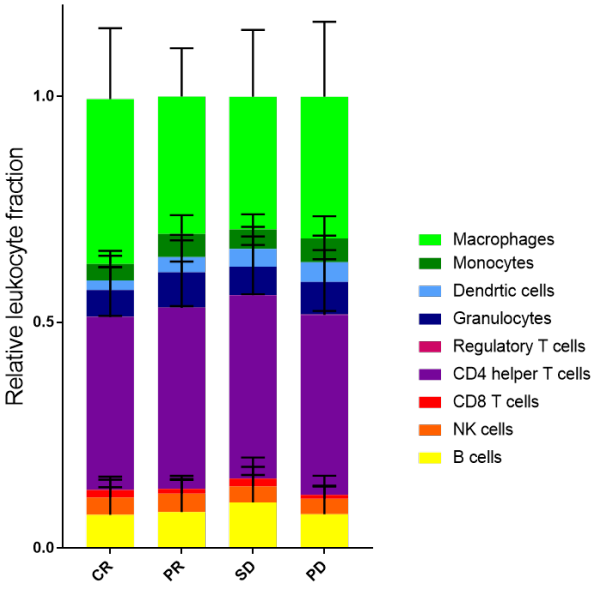

Supplementary Fig. 9: CIBERSORT stacked graph of overall cell populations in atezolizumab patient cohort. CIBERSORT cell subsets were condensed into 9 key subsets and plotted as a stacked graph for each response type (CR, Complete Response; PR, Partial Response; SD, Stable Disease; PD, Progressive Disease).

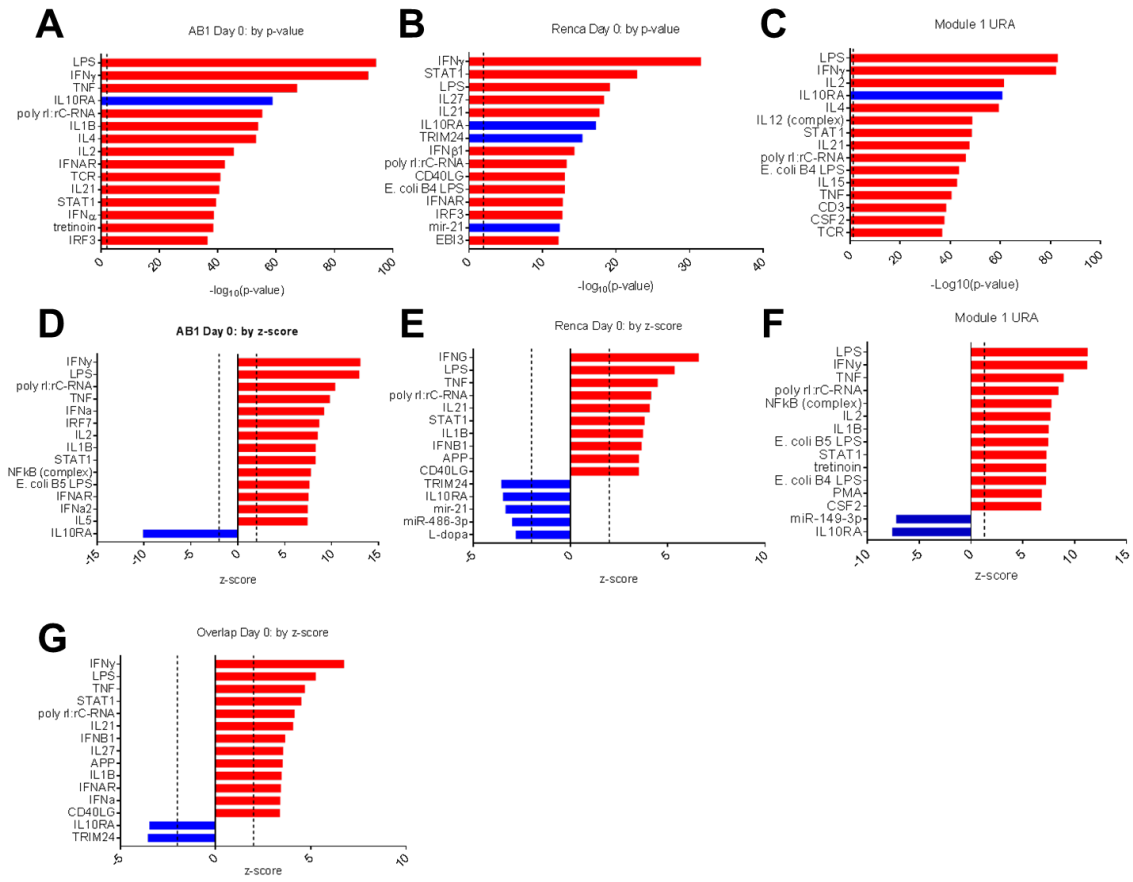

Supplementary Fig. 10: Upstream regulator analysis of differentially expressed genes in AB1, Renca, and module 1 (combined AB1 and Renca) by p-value and z-score. Both AB1 (**A**) and Renca (**B**) URA by p-value resulted in similar target outputs. The module 1 URA by p-value (**C**) also resulted in a similar output, reinforcing this module is central to the response. The respective analyses are also shown ranked by z-score (**D-F**). All 3 analyses identified IFNγ and Poly(I:C) as top positive regulators, and IL-10 as a top negative regulator. URA of the overlap of DE genes (AB1 and Renca) by p-value shown in **figure 4A**, and by z-score (**G**) (Positive regulators in red, negative regulators in blue (by z-score); dashed line; p = 0.05).

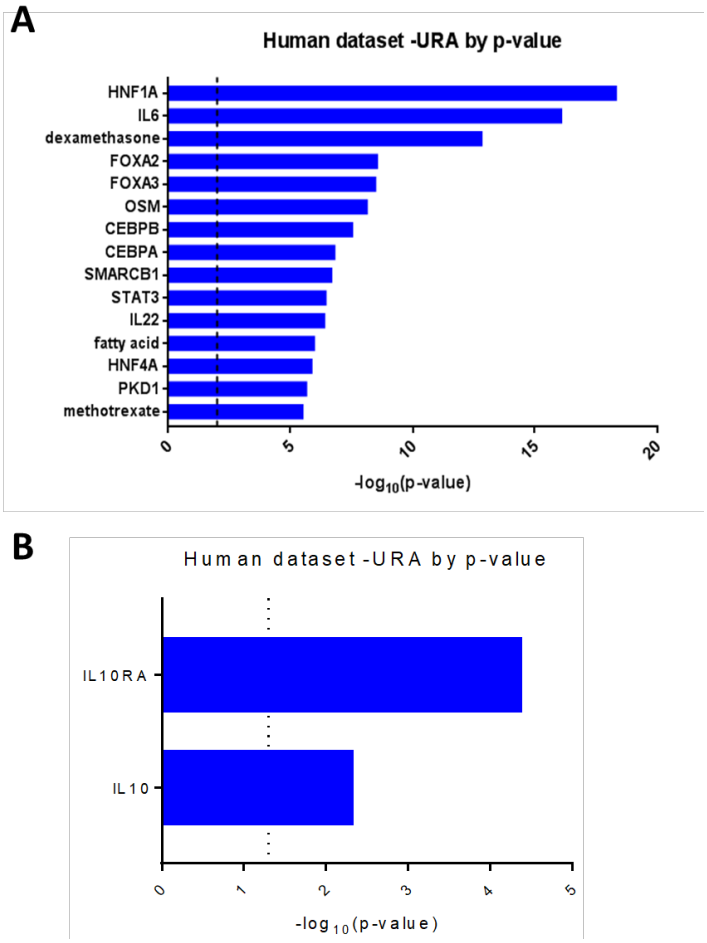

Supplementary Fig. 11: Upstream regulator analysis of the atezolizumab cohort, negative regulators. Analysis of the urothelial cancer/atezolizumab dataset identified several significant negative upstream regulators. (**A**) The top 15 negative regulators. (**B**) The top negative regulator, IL-10RA, identified in the mouse dataset, is also a significant negative regulator in the human dataset (dashed line; p = 0.05).

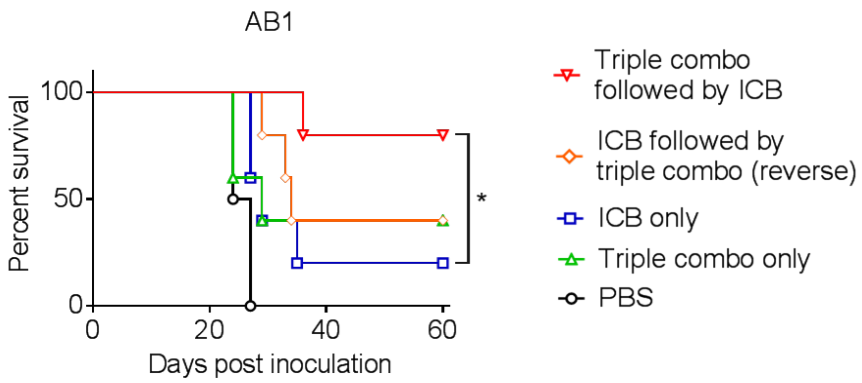

Supplementary Fig. 12: Sequencing of treatments determines anti-tumor efficacy of combination immunotherapy. To determine whether the triple combination was sensitizing the tumor to ICB, rather than enforcing the effector response, the triple combination followed by ICB was compared to ICB followed by the triple combo. Demonstrated in AB1 n=5/group (Logrank test, *p< 0.05, **p< 0.01).

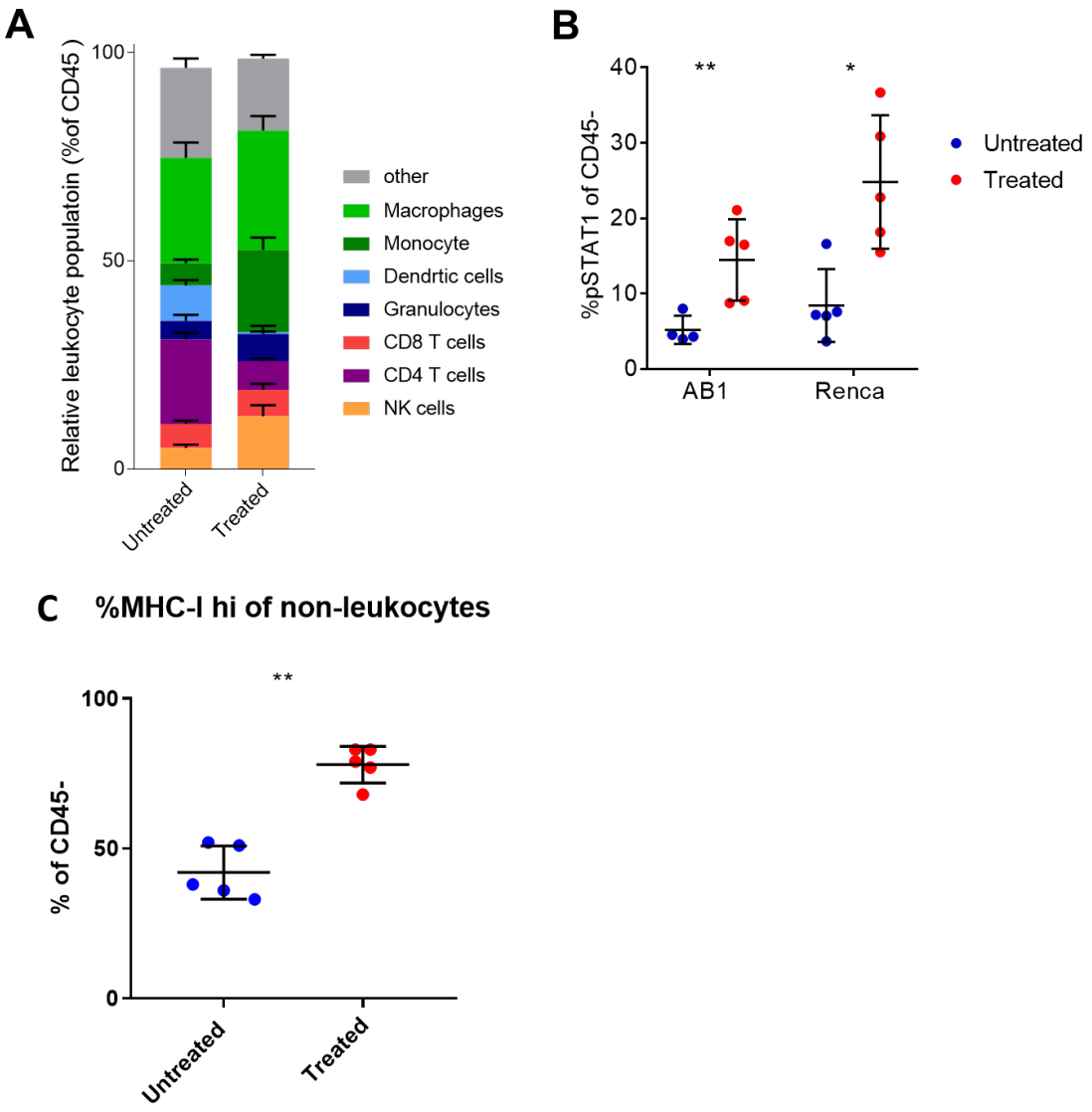

Supplementary Fig. 13: Flow cytometry analysis after treatment with IFNγ + Poly(I:C) + anti-IL-10. To determine if the predicted upstream regulators could induce a responder phenotype, we analyzed treated tumors by flow cytometry**.** Treating large established tumors with IFNγ, Poly(I:C) and anti-IL-10 resulted in a phenotype similar to pre-treatment responsive tumors. (**A**) Treatment increased the proportion of NK cells infiltrating the tumor, characteristic of a responsive tumor (see **Fig. 3**). We also observed increased monocytes, and decreased $CD4^+$ T cells and dendritic cells (n=9 per group, 2 individual experiments, Renca). (**B, C**) In addition to increased pSTAT1 on $CD45^+$ leukocytes (**Fig. 5B**), we also observed increased pSTAT1 (B) and MHC-I (C, Renca) expression in non-leukocytes ($CD45^-$ tumor cells and stroma) after treatment (Mann-Whitney U test) *p< 0.05, **p< 0.01

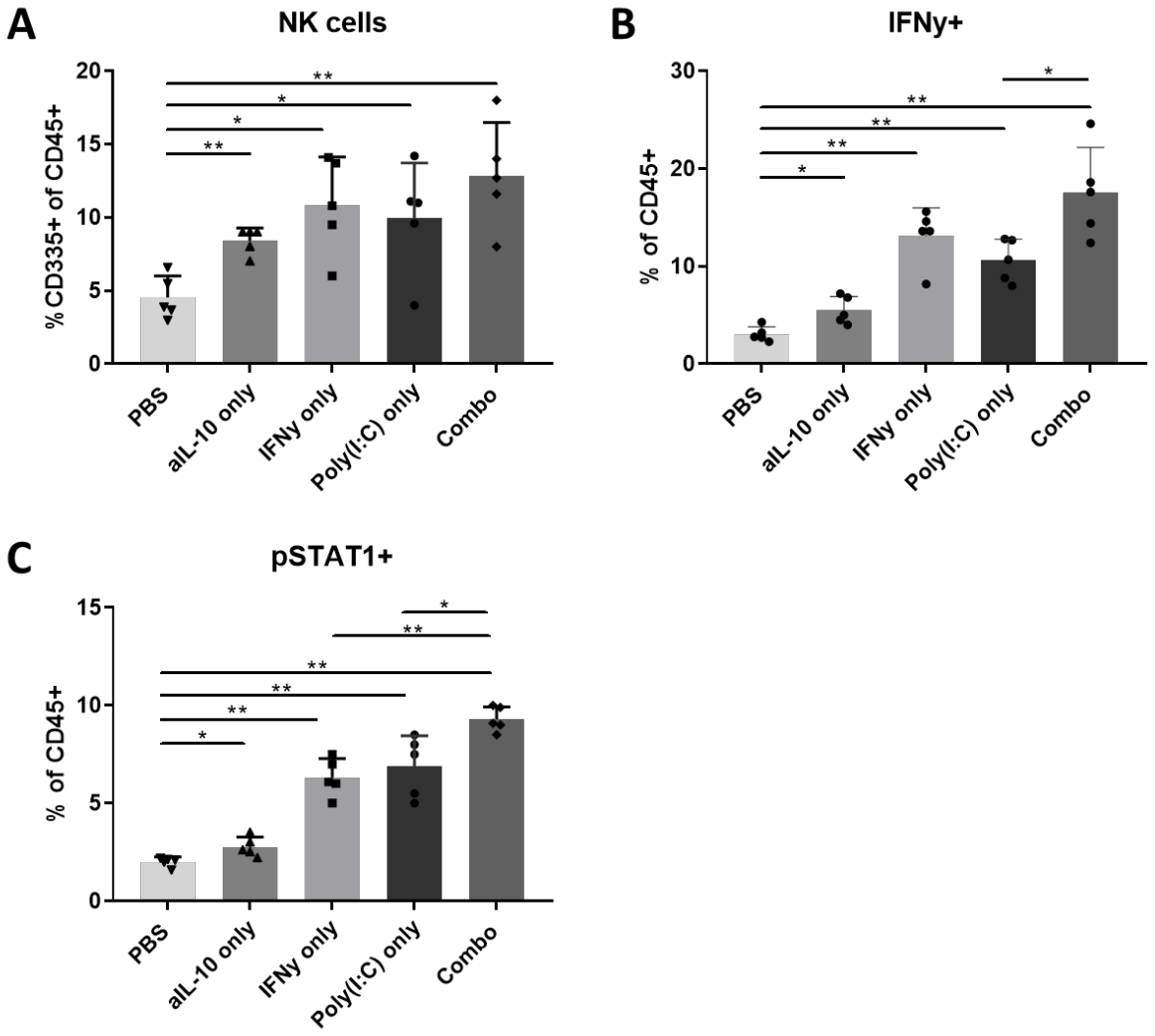

Supplementary Fig. 14: Flow cytometric analysis of single-agent compared to triple-agent treated tumors. (**A**) All 3 agents are able to recruit NK cells to the tumor microenvironment, with the greatest effect given by the triple combination. (**B**) The triple combination induces the most IFNy expression, significantly more than poly(I:C) or IL-10 alone. (**C**) The triple combination induces significantly more pSTAT1 than any of the agents alone. (Mann-Whitney U test) *p< 0.05, **p< 0.01

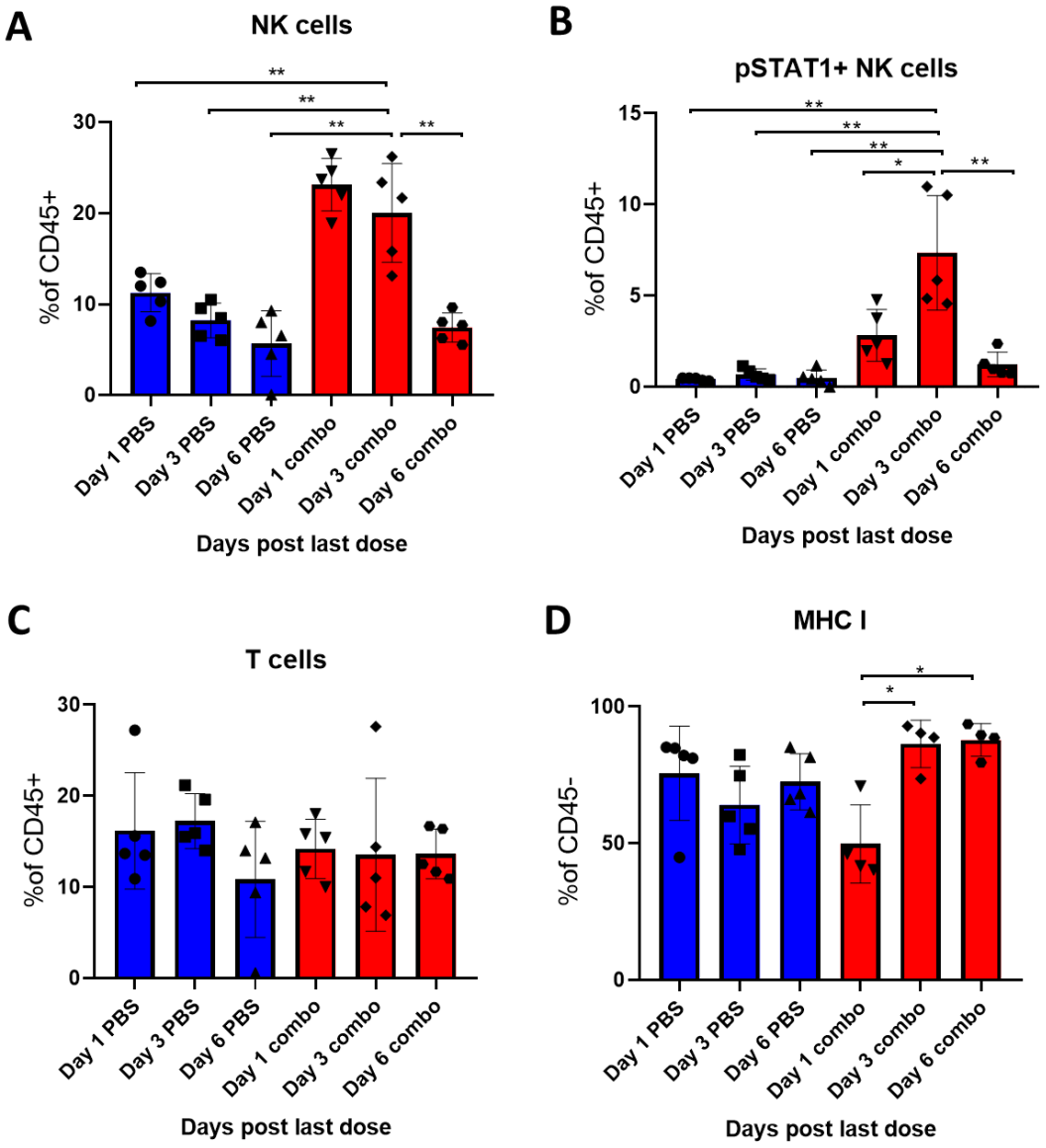

Supplementary Fig. 15: Analysis of tumors 1-, 3- or 6-days post triple-combination by flow cytometry. We characterized the tumor microenvironment at three different time points after the final pretreatment dose. (A) There is initial rapid NK cell infiltration on day 1-3, followed by a decrease on day 6. (B) The number of pSTAT1+ NK cells increased on days 1-3, with significantly more on day 3. (C) There is no difference in $CD3^+$ T cell infiltration between treated and untreated tumors, nor between time-points. (D) MHC class I is initially downregulated 1-day post-pretreatment, and then upregulated on days 3-6 (D). These results suggest it would be optimal to start ICB early after pretreatment (Mann-Whitney U test *p< 0.05, **p< 0.01).

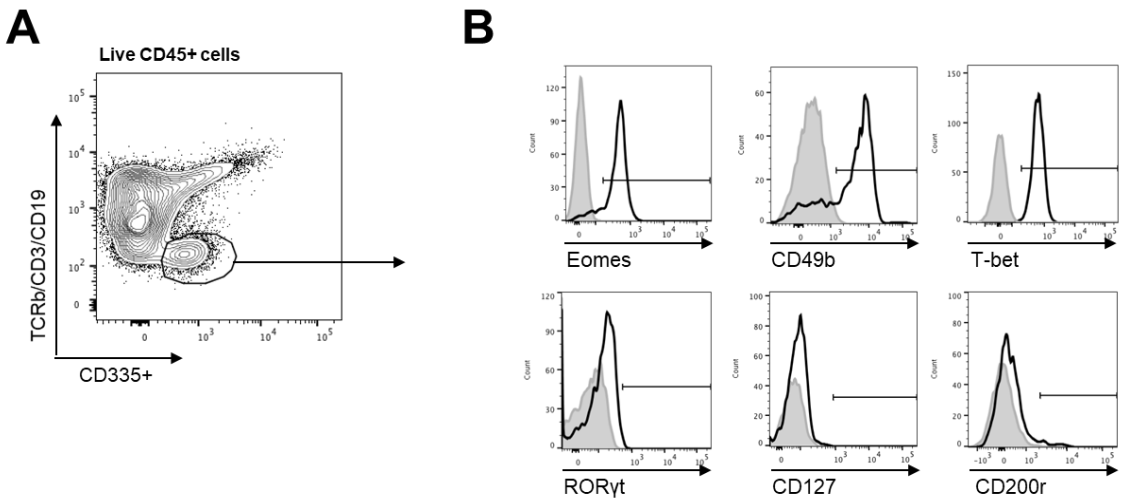

Supplementary Fig. 16: CD335^{+} cells in tumors are conventional NK cells. To determine the phenotype of CD335^{+} cells in tumors we performed flow cytometric analysis of live CD45^{+} CD3^{-} TCRb^{-} CD19^{-} CD335^{+} cells (**A**). The CD335^{+} population primarily expressed the NK cell-specific markers Eomes and CD49b. Cells also expressed T-bet, while lacking the ILC3 marker RORγt and the ILC1 markers CD127 and CD200r (**B**). Plots in (**A**) and (**B**) are representative of both untreated (n=4) and treated (n=5) tumors. Representative samples (black open histogram) are overlayed with staining controls (grey tinted histogram) for each marker.

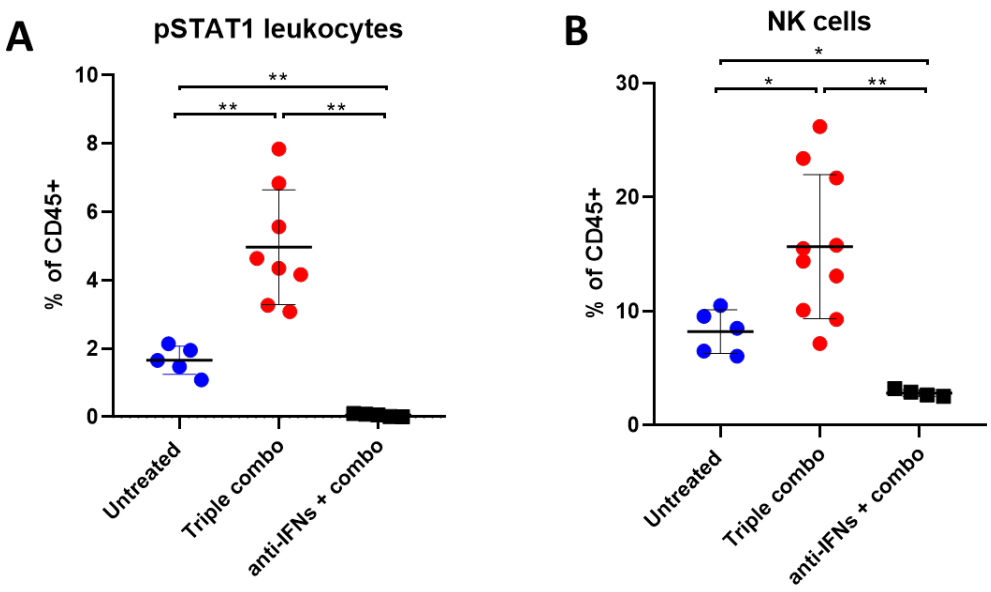

Supplementary Fig. 17: The IFN-STAT1 pathway is required for NK cell infiltration. To further substantiate the role of STAT1 in the sensitizing effect of the triple combination therapy, we blocked IFNy and IFNAR with antibodies, which are both upstream of STAT1, and repeated the analysis of the response-associated signature by flow cytometry following pre-treatment. (A) Phosphorylation of STAT1 was abrogated by blocking type I and II IFN, confirming full inhibition of the STAT1 pathway. (B) This functional STAT1 blockade abrogated NK cell infiltration in the tumors (Mann-Whitney U test, *p< 0.05, **p< 0.01).

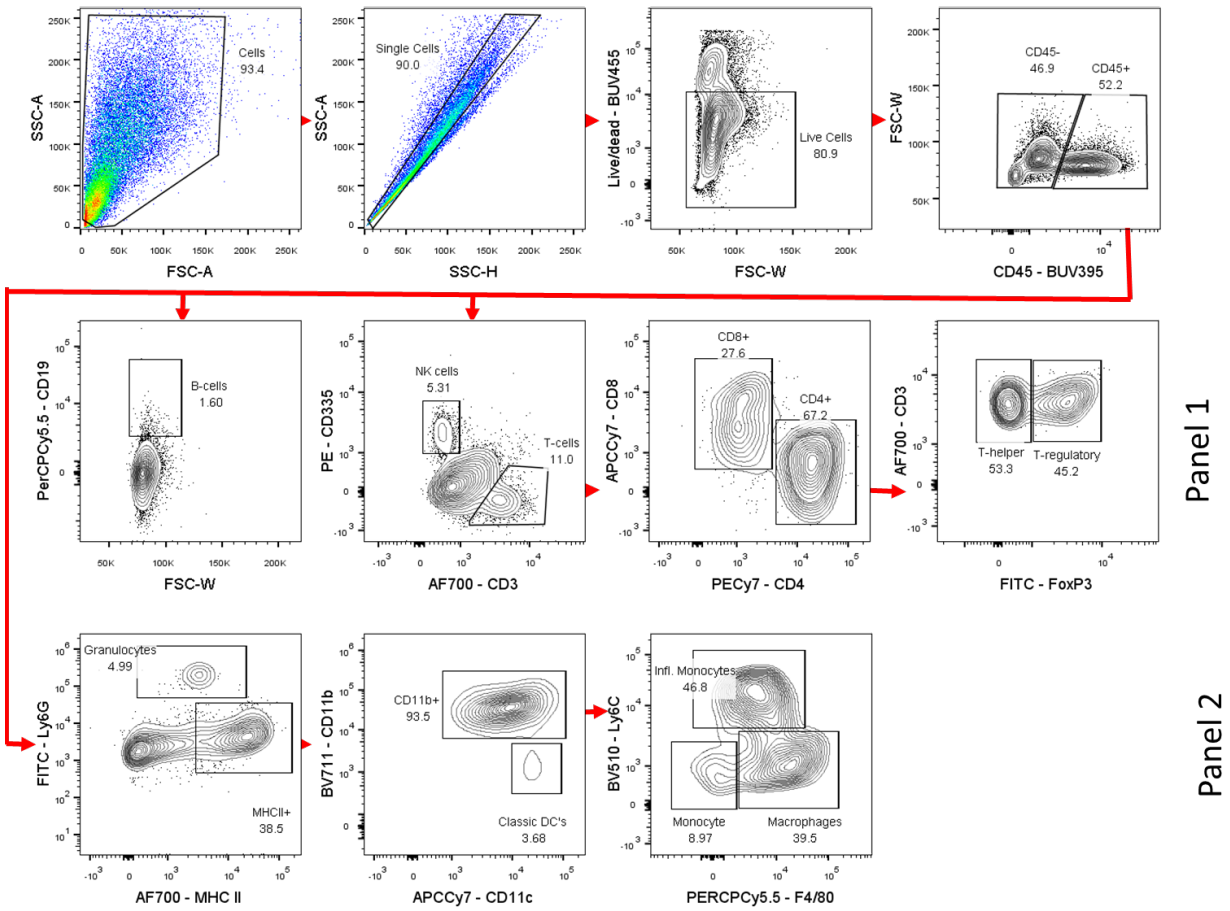

Supplementary Data Fig. 18: Flow cytometry gating strategy.

Fluorophore	Antibody	Clone	Vendor
BUV455	**UV Zombie live-dead**		BD
BUV395	**CD45**	30F11	Biolegend
AF700	**CD3**	17A2	Biolegend
APCCy7	**CD8**	53-6.7	Biolegend
PECy7	**CD4**	RM4-5	Biolegend
FITC	**Foxp3**	FJK16s	ThermoFisher
PE	**CD335 (Nkp46)**	29A1.4	Biolegend
APC	**CD278 (ICOS)**	C398.4A	Biolegend
BV605	**Ki67**	16A8	Biolegend
PerCPCy5.5	**CD19**	6DS	Biolegend
AF700	**I-A/I-E (MHC-II)**	M5/114.15.2	Biolegend
APCCy7	**CD11c**	N418	Biolegend
BV711	**CD11b**	M1/70	Biolegend
FITC	**Ly6G**	1A8	Biolegend
BV510	**Ly6C**	HK1.4	Biolegend
PerCPCy5.5	**F4/80**	BM8	Biolegend
PE	**pSTAT1**	Y701	Cell Signaling Technology
(Fc-block)	**anti-CD16/CD32**	2/04/1900	Biolegend
620 (PE-CF594)	**Fixable Viability Stain 620**		BD
APCCy7	**CD45**	30F11	BD
TCRb PerCPCy5.5	**TCRb**	H57-597	BD
BV650	**CD8**	53-6.7	BD
APC	**CD4**	RM4-5	BD
V500	**MHC II**	M5/114.15.2	BD
BV605	**Ly6G**	1A8	BD
BV786	**CD11c**	HL3	BD
AF700	**Ly6C**	AL21	BD
BV711	**F4/80**	BM8	Biolegend
FITC	**CD11b**	M1/70	Biolegend
PECy7	**CD335 (Nkp46)**	29A1.4	ThermoFisher
PE	**IFNy**	XMG1.2	ThermoFisher
BV421	**CD127**	A7R34	BD
BV510	**CD11b**	M1/70	BD
BV605	**Tbet**	4B10	Biolegend
BV711	**CD49a**	Ha31/8	BD
biotin	**CD49b**	DX5	BD
FITC	**CD3**	145-2C11	BD
FITC	**CD19**	6D5	Biolegend
FITC	**TCRb**	H57-597	BD
PE	**RORgt**	B2D	ThermoFisher
PerCPeFluor710	**Eomes**	Dan11mag	ThermoFisher
APC	**CD200R**	OX110	ThermoFisher
AF700	**IFNg**	XMG1.2	BD
SA-BV786			BD

Supplementary Table 1: Flow cytometry antibodies.